

UNIVERSITATEA „BABEȘ-BOLYAI” CLUJ-NAPOCA

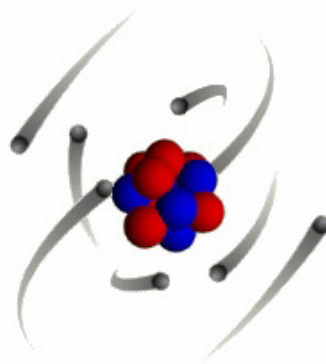
FACULTATEA DE FIZICĂ



PHD. THESIS SUMMARY

*Electronic structure and magnetic
properties of metallic systems
based on rare earths and d
transition elements*

Lidia Rędnic



SCIENTIFIC SUPERVISOR

Prof. Dr. Marin Coldea

CLUJ NAPOCA
2010

THESIS CONTENT

Introduction	1
1. Theoretical aspects	
1.1. General issues of magnetism	4
1.1.1. The origin of atomic moments	4
1.1.2. Main classes of magnetic behaviour	7
<i>Diamagnetism</i>	7
<i>Paramagnetism</i>	7
<i>Ferromagnetism</i>	8
<i>Antiferromagnetism</i>	9
<i>Ferrimagnetism</i>	10
1.1.3. Microscopic bases of magnetism	10
1.1.3.1. Exchange interactions	10
<i>Direct exchange</i>	11
<i>Indirect exchange</i>	12
1.1.3.2. Localized magnetic moments	12
1.1.3.3. Itinerant -electron magnetism	13
<i>Stoner model</i>	14
1.1.3.4. Local magnetic moments	17
<i>Virtual bond state model (Friedel)</i>	18
<i>Anderson model</i>	20
<i>Interactions between localized magnetic moments</i>	23
1.1.4. Magnetism of <i>3d</i> metals	24
1.1.5. Rare-earths magnetism	27
1.1.6. Coupling exchange mechanism in rare earth - transition metal (R-T) compounds	28
1.2. X-ray Photoelectron Spectroscopy (XPS)	30
1.2.1. Physical bases of the XPS method	30

1.2.2. Theoretical models of photoemission process	31
<i>Three-step model of photoemission</i>	32
<i>One step model of photoemission</i>	33
1.2.3. General Characteristics of XPS spectra – data analysis	33
1.2.3.1. Acquiring of XPS spectra	33
1.2.3.2. Valence band spectra	34
1.2.3.3. Core level spectra	34
<i>Spin-orbit splitting</i>	34
<i>Intensity and line shape</i>	35
<i>Multiplet splitting</i>	36
<i>Chemical shifts</i>	37
<i>Satellite lines</i>	37
<i>Secondary XPS spectra (Background)</i>	38
2. Measurement devices and experimental methods used for	41
sample characterization	
2.1. Structural characterisation - Brucker D8 Advance diffractometer	41
2.2. Instrumentation used for magnetic behaviour characterisation	42
2.2.1. Weiss balance	42
2.2.2. MagLab system 2000 cryostat	46
(Oxford Instruments)	
2.2.3. Vibrating sample magnetometer (VSM)	47
2.2.4. Superconducting quantum interfering device	49
(SQUID magnetometer)	
2.3. Instrumentation used for XPS measurements	49
<i>Vacuum conditions</i>	50
<i>X-ray source</i>	50
<i>Monochromator</i>	51
<i>Analyser</i>	51
<i>Ion gun</i>	52
<i>Neutraliser</i>	52
2.4. Electronic structure calculation	53

3. Experimental results and discussions	55
3.1. Magnetic cluster development in $In_{1-x}Mn_xSb$	55
($x=0, 0.05, 0.1, 0.15$ and 0.2) system	
3.1.1. Sample preparation and structural characterisation	57
3.1.2. TEM analysis	59
3.1.3. Magnetic measurements	59
3.1.4. XPS spectra	66
3.1.5. Summary	73
3.2. Magnetic cluster development in oxidized	74
$CeNi_5$ powder	
3.2.1. Synthesis and structural characterisation	75
3.2.2. TEM analysis	84
3.2.3. Magnetic measurements	84
3.2.4. XPS spectra	87
3.2.5. Raman measurements	90
3.2.6. Summary	91
3.3. Electronic structure and magnetic properties of some	92
compounds belonging to the ternary $Al-Dy-Ni$ metallic system	
($AlDyNi, AlDyNi_4$ and $AlDy_3Ni_8$)	
3.3.1. Sample preparation and structural characterisation	92
3.3.2. Magnetic measurements	94
3.3.3. XPS spectra	99
3.3.4. Summary	102
3.4. Electronic structure and magnetic properties of	102
$MnSb_{1-x}Bi_x$ ($x= 0, 0.2, 0.5$ and 0.95) system	
3.4.1. Sample preparation and structural characterisation	103
3.4.2. Magnetic measurements	105
3.4.3. XPS spectra	107
3.4.4. Summary	113
References	115
List of figures	121

List of tables	124
List of publications	125
List of conference contributions	127
Acknowledgements	

Keywords: magnetic measurements, magnetic semiconductors, local magnetic moments, X-ray diffraction, XPS spectra

INTRODUCTION

Solid state magnetism represented and continues to be a broad interest area of Physics because of the many possibilities it offers in theoretical investigations and technical applications.

The investigation of electronic structure and magnetic properties of metallic systems based on rare-earths and $3d$ transition elements occupy a very special place in *Solid State Physics*, since this type of materials have fascinated and continue to attract the interest of scientific community and industry since their properties can be modified and developed for applications such as spin controlled electronic devices, high-density permanent magnets, magnetic storage media or giant magnetoresistive alloys for technological applications.

Understanding and prediction of mater properties, at atomic level, represents one of the great achievements of the last years in science. In this content, the advantage of photoelectron spectroscopy, in the study of electronic structure and properties of matter is due to progress in both, experimental and in relevant theory. Photoemission techniques have been developed sufficiently to become a major tool for the experimental studies of solids. These techniques are also attractive for the study of changes in, or destruction of, crystalline order. A profound magnetic behaviour understanding cannot be achieved without a thorough study of electronic structure.

Knowing the electronic structure of metallic systems based on d transition elements and implicitly the valence band structure represents one of the fundamental problems in understanding the mechanisms of magnetic interactions in $3d$ intermetallic compounds. One of the most important and widely used techniques to study the energy spectra of solids is the *X-Ray Photoelectron Spectroscopy (XPS)*.

The correlation of *XPS* data with magnetic measurements as a function of applied field and temperature, together with band structure calculations provide clear information regarding the intensity of magnetic interactions in these materials.

The subject of present work subscribes to the international preoccupation regarding the elucidation of magnetic properties of solids and how these properties depend on the electronic energy spectrum and how can they be modified trough alloying. For this purpose, several classes of materials based on rare-earths and $3d$ transition elements have been studied:

- **Compounds belonging to $In_{1-x}Mn_xSb$ ($x=0, 0.05, 0.1, 0.15$ and 0.2) system**
- **Oxidized $CeNi_5$ powder**
- **Compounds belonging to $Al-Dy-Ni$ ($AlDyNi$, $AlDyNi_4$ and $AlDy_3Ni_8$) system**
- **Compounds belonging to $MnSb_{1-x}Bi_x$ ($x=0, 0.2, 0.5$ and 0.95) system**

The thesis is organized in three main chapters and includes a selective bibliography inserting **158** indexes.

The first chapter is divided in two and covers the theoretical bases that form the basis in explaining and understanding the magnetic behaviour of investigated materials. Here are listed all theoretical models used, $3d$ transition metals and rare-earths magnetism, as well as the underlying

phenomena in *X-ray Photoelectron Spectroscopy*, used in energy spectrum evaluation, together with the main spectral features corresponding to a *XPS* spectrum

The second chapter is devoted to the description of all installations used in structural determination, recording of magnetic data necessary in order to elucidate the magnetic behaviour, as well as ESCA PHI 5600 spectrometer used to characterize investigated samples in terms of spectroscopic evidence.

The third and final chapter is divided into four sub-chapters corresponding to four different classes of materials. Here are presented and analyzed the X-ray diffraction (*XRD*), transmission electron microscopy (*TEM*), magnetic measurements as a function of applied external field and temperature, valence band and core level *XPS* spectra results, correlated with band structure calculations.

CHAPTER 1

Theoretical aspects

1.1. Magnetic properties of metallic systems

The most direct evidence of **magnetism** is the attraction or repulsion force between elements. The origin of magnetic forces lays in the orbital and spin rotation of electrons around the nucleus. The modern theory of magnetism can be divided in:

- *atomic magnetism* (generated by the electrons movement around the nucleus), which deals with magnetic properties of elementary particles, atomic nucleus and electronic shells of isolated atoms or molecules
- *condense matter magnetism* which treats the magnetic properties of systems formed by atoms or molecules which interacts with each other.

In the first situation magnetic properties of isolated magnetic carriers are studied, while the magnetic properties of materials and magnetic moment interactions are investigated in the second case.

Pauli's exclusion principle postulates that it is not possible for two electrons to occupy the same state, therefore each electron can occupy a different energetic level or quantum state which can be defined by a set of five unique numbers: n , l , m_l , s and m_s .

By analyzing their response to the action of an external magnetic field the magnetic one can distinguish the following magnetic behaviors: *diamagnetism*, *paramagnetism*, *ferromagnetism*, *antiferromagnetism* and *ferrimagnetism*. The materials belonging to the first two groups do not exhibit collective magnetic interactions and are not magnetically ordered, while the materials in the last three groups exhibit long-range magnetic order below a certain critical temperature.

There are two classes of elements which play an important role in magnetism: transition metals (*3d*) and rare earths (*4f*). For the elements belonging to these two series, the unfilled electronic shells (*3d* and *4f* respectively) are not outer shells and can remain unfilled even in solids, leading to the appearance

of magnetism. In order to explain the magnetic properties of metallic systems based on $3d$ transition elements two complementary models were developed: itinerant and localised. The nonintegral values of magnetic moment per atom, the high values of specific electronic heat coefficient which are not compatible with localized model, impose the use of itinerant model in case of transition metals and their alloys. But, this model cannot explain the *Curie-Weiss* law observed for all ferromagnetic metals for $T > T_C$, and the calculated value of *Curie* temperature is too big comparing to the experimental one, problems that are easily resolved by localized model. The *Fermi* surfaces associated to the d electrons from magnetic transition metals, the success of band structure calculations in the reproduction of these surfaces and the explanation of magnetic properties in the fundamental state sustain the importance of using itinerant model in case of transition metals magnetism. The reconciliation between these two models was made by considering the atomic character of $3d$ band electrons around each atomic position and the interatomic exchange interactions (strongly correlated d itinerant electrons)

The interaction between magnetic moments, called **exchange interaction**, originates in the correlation of electrons belonging to different atoms. The magnetic coupling is usually described using the *Heisenberg* Hamiltonian: $H = -2J\vec{S}_i \cdot \vec{S}_j$, where J is the exchange integral which depends on the charge distribution of i and j atoms. A spin operator of this form was first deduced from the *Heitler-London* results by *Dirac* [1] and first extensively applied in the theory of magnetism by *Van Vleck* [2]. If the orbitals of two neighbour atoms present a sufficient space extension so that a overlap is possible, the correlation effects lead to a direct interaction between the atoms spins. This phenomenon is known as **direct exchange**. The direct exchange is characteristic for $3d$ intermetallic compounds, and represents the stronger interatomic interaction, being responsible for the magnetic order up to high temperatures. When magnetic orbitals of two neighboring atoms are too localized to overlap, as in the case for the $4f$ series, the exchange process can occur through conduction electrons if the system is metallic. This leads to an **indirect exchange** of *RKKY* type (*Ruderman, Kittel, Kasuya, Yosida*) [3-5].

The theory of ferromagnetism is in a far from satisfactory state. Actually, there is not a single theory, but at least two rather divergent viewpoints: (1) the localized moment theory, and (2) the band models. According to the localized moment theory, the electrons responsible for magnetism are attached to the atoms and cannot move into the crystal. These electrons generate a certain magnetic moment which is localized at the position of each atom. This view is implicit in the molecular field theory, either in the original form given by *Weiss* [6] or in the quantum-mechanical form obtained by substituting the *Brillouin* function for the *Langevin* [7].

Opposite to the localized model is the itinerant (or band) model which considers that the magnetic carrier are the so called *Bloch* electrons which are itinerant through the solid, and the exchange interaction leads to a difference between the number of spin up and down electrons. The simplest model of itinerant-electron magnetism is the Stoner model [8, 9], which has mainly been used to account for the existence of ferromagnetism in itinerant systems. Both localized model and itinerant model fail to fully describe the magnetic behaviour of magnetic transition metals. It is very clear that d electrons should be treated as localized electrons in magnetic insulator compounds and as correlated itinerant electrons in transition metals. There have been two main directions in the attempt of reconciliation between these two models:

one was to improve the *Stoner* theory by considering the electron-electron correlation, and the other was to start with the study of local moments in metals. *Van Vleck* [10] discussed the justification of local moments, considering the importance of electron correlation in narrow *d* bands. An explicit model describing the local moments in metals was proposed by *Anderson* [11] on the basis of the *Friedel* picture of virtual bound states in dilute magnetic alloys [12]. The interaction between local moments in metals was studied by *Alexander* and *Anderson* [13] and by *Moriya* [14] on the basis of the *Anderson* model.

1.2. *X-Ray Photoelectron Spectroscopy (XPS)*

X-Ray Photoelectron Spectroscopy (XPS) was developed in the mid 1960's by *K. Siegbahn* and his research group from the University of Upsalla, Sweden [15, 16]. The technique is based on the photoelectric effect outlined by *Einstein* in 1905 and is a failure analysis technique primarily used in the identification of elements from the sample surface. The analysis is done by irradiating a sample with soft X-rays to ionize atoms and releasing core-level photoelectrons. The usually used radiations are those of aluminium (*Al K-alpha* $E = 1.487$ keV) and magnesium (*Mg K-alpha* $E = 1.254$ keV). Although X radiations penetrate deep into the sample, the important information regarding the electronic structure of the solid is given only by those electrons who manage to reach the surface without any energetic loss due to inelastic scattering processes. A rigorous description of photoemission process implies a quantum description of this process which consists in the emission of an electron from the inner shells of a solid, the detection of the photoelectron is made after it leaves the sample surface. The most known theoretical model of the photoemission process is the so called “**three-step model**” developed *Spicer* in 1985 [17]. In 1964 *Berglund* and *Spicer*, published a more sophisticated formalization of the same model [18]. Along the time there were developed many theories that tried to explain the photoemission process, in present the most used of them is the one known as “**one step model**”. *XPS* can detect all elements except *H* and *He* (owing to the absence of the core orbital). An *XPS* spectrum is displayed as a plot of electron binding energy versus the number of electrons in a fixed energy interval and can be divided in two parts:

- **primary spectrum** – generated by the electrons who are leaving the solid without suffering inelastic scattering processes
- **secondary spectrum (background)** – formed by the photoelectrons who have lost a percentage of their kinetic energy due to inelastic scattering processes

There are various spectral features that are likely to be encountered in a *XPS* spectrum. Some are fundamental to the technique, and are always observed, and others are dependent upon the chemical and physical nature of the sample. Valence band levels appear as lines of low intensity in the low binding energy region of the *XPS* spectrum, between the *Fermi* level and about 10-15 eV binding energy. These energetic levels are very important in explaining the properties of solids because one can determine the band structure considering only the direct transitions that can happen without any other external excitation. *XPS* measures the transitions between these occupied and the unoccupied states and offer important information about the occupied states in the valence band region. The *Fermi* level position gives us information about vacant states from the valence band and curve's slope near *Fermi* level is a

measure of the states density. The electrons from the most inner shells of the atoms give rise to the most intense and well define lines in the *XPS* spectrum. A closer inspection of the spectrum shows that emission from some levels does not give rise to a single photoemission peak, but a closely spaced doublet, due to spin-orbit splitting. The exact binding energy of an electron depends not only upon the level from which photoemission is occurring, but also upon: formal oxidation state of the atom, local, chemical and physical environment. Changes in these states give rise to small shifts in the peak positions - so-called **chemical shifts** [19]. In the photoemission process the photon kicks out the electron so quickly that the remaining electrons do not have time to readjust. The reorganization of the electrons upon the core-hole can lead to electronically excited final states. This means that the *XPS* spectrum will consist from the main line which corresponds to the lowest excited state and a number of additional lines, so-called **satellites**, which correspond to the higher excited state after the photoemission.

CHAPTER 2

Measurement devices and experimental methods used for sample characterization

2.1. Structural characterization - Bruker D8 Advance Diffractometer

After preparation, the crystallographic structure of all investigated samples was checked at room temperature using *X-ray powder diffraction (XRD)* data. Small pices of the as-prepared samples were crushed and the obtained powder was analysed at room temperature using *Cu K α* radiation of a *Bruker D8 Advance* diffractometer. The operation method used by the diffractometer is the *Bragg-Brentano* geometry [20]. The data recorded in the detector is the X-ray intensity in counts/second. By plotting the intensity against the angle of the incident X-ray, we can produce a series of peaks. The acquired data were analysed using *PowderCell 2.3*.program [21].

2.2. Instrumentation used for magnetic behaviour characterisation

The magnetic properties were studied trough static and dynamic magnetic measurements in the 4.2 – 900 K temperature range and fields up to 8 T. At low temperatures (< 300 K) several devices were used: vibrating sample magnetometer (*VSM*), *SQUID* magnetometer and the *MagLab* system 2000 cryostat (*Oxford instruments*). At high temperatures (higher than the corresponding transition temperature) a *Weiss* balance was used in order to determine the variation of magnetic susceptibility with temperature. The magnetic measurements were performed in France at *Laboratoire de Crystallographie CNRS, Grenoble* and *Institute des Matériaux Jean Rouxel, Nantes*, but also in Cluj in the *Solid State laboratories of Ioan Ursu Institute*.

2.3. Instrumentation used for XPS measurements

The electronic structure of investigated alloys is studied by means of *X-Ray Photoelectron Spectroscopy*, analyzing the valence band and core level spectra. XPS measurements were performed in Germany, at *Osnabrück Universität*, using the *ESCA PHI 5600* spectrometer manufactured by *Perkin Elmer Corporation*, belonging to *A.G. Neumann*. All the spectra were recorded at room temperature, using a monochromatized *Al K- α* source. The pressure in the ultra-high vacuum chamber was in the 10^{-10} mbar range during the measurements. The samples were cleaved in situ. The surface cleanness was checked by monitoring the *O 1s* and *C 1s* core levels in the survey spectra.

2.4. Band structure calculations

Electronic structure theoretical investigations for some of the investigated samples have been performed using the *Munich SPR-KKR package version 3.6* [22]. The electronic structures were calculated self-consistently by means of the spin polarized relativistic *Korringa–Kohn–Rostocker* (SPR-KKR) method in the atomic sphere approximation (ASA) mode [23-25].

CHAPTER 3

Rezultate experimentale

3.1. Magnetic cluster development in $In_{1-x}Mn_xSb$ ($x=0, 0.05, 0.1, 0.15$ and 0.2) system [26, 27]

The doping of *III-V* semiconductors with *3d* transition elements creates ferromagnets, called **magnetic semiconductors**. These materials continue to attract the interest of scientific community, since they hold promise of applications in a variety of spin-controlled devices [28].

InSb is a narrow gap semiconductor with an energy band gap of 0.17 eV at 300 K and 0.23 eV at 80 K. It crystallizes in the zinc-blende structure type with a 0.648 nm lattice constant. The undoped semiconductor possesses the largest ambient temperature electron mobility (7.8 $m^2V^{-1}s^{-1}$), electron velocity, and ballistic length (up to 0.7 μm at 300 K) of any known semiconductor [29].

Ferromagnetism in $In_{1-x}Mn_xSb$ ($x \sim 0.02$) with T_c up to 20 K has been observed in films grown by *Molecular Beam Epitaxy* (MEB) [30]. Earlier studies on bulk $In_{1-x}Mn_xSb$, performed in the $0.01 \leq x \leq 0.06$ concentration range [31]. In order to complete the picture and explain the magnetic behaviour of these materials a study of bulk manganese-doped *InSb*, for higher manganese concentration, was necessary.

Manganese was chosen as doping element due to its unique electronic structure $3d^54s^2$. It is particularly interesting because, according to Hund's rule, in case of the free atom there is the possibility to obtain a maximum value of the spin, of about $5\mu_B$. The substitution of *In* by *Mn* in *InSb* can lead to a partial or total filling of the *3d* band and the localisation/delocalisation degree of *3d* electrons undergoes changes. In bulk materials the value of magnetic moments localized at the position of transition element and the interactions between such moments, which lead to ordered magnetic behaviour, depend on *Mn-Mn* distances, manganese atoms vicinity (the number of neighbours with *3d* orbitals), hybridization

degree between $3d$ orbitals of Mn atoms, also the hybridization between $3d$ orbitals and other orbitals belonging to different element which enter in the composition of the alloy or intermetallic compound, conduction electrons per atom concentration. In intermetallic compounds, the values of local magnetic moments, the nature and intensity of magnetic interactions, depend on crystallographic structure. The vicinity effects study on local magnetic moments at Mn position is very important in order to obtain improved materials and explain their magnetic behaviour.

The doping of $InSb$ with Mn , beyond the solid solubility limit, leads to the formation of several phases: ferromagnetic $In_{1-x}Mn_xSb$ solid solution, ferromagnetic $MnSb$ and ferrimagnetic Mn_2Sb phases.

3.1.1. Samples preparation and structural characterisation

Five samples belonging to $In_{1-x}Mn_xSb$ system were prepared by argon arc melting method. High purity elements have been used for the samples preparation (99.99% for both In and Mn and 99.9% in case of Sb). In order to aid homogenization the samples were inverted and re-melted several times in the same atmosphere. The weight loss of the final samples was found to be less than 1%. Investigated samples have the following Mn concentrations: $x=0, 0.05, 0.1, 0.15$ and 0.2 . $InSb$ crystallizes in a zinc-blende (ZnS) structure type with the lattice parameter $a = 6.48 \text{ \AA}$. $MnSb$ crystallizes in a $NiAs$ structure type with the following lattice parameters: $a = 4.5285 \text{ \AA}$ and $b = 5.9311 \text{ \AA}$ [32, 33], and Mn_2Sb present also a $NiAs$ structure with $a = 4.0800 \text{ \AA}$ and $b = 6.5600 \text{ \AA}$ [34] (Fig. 1.).

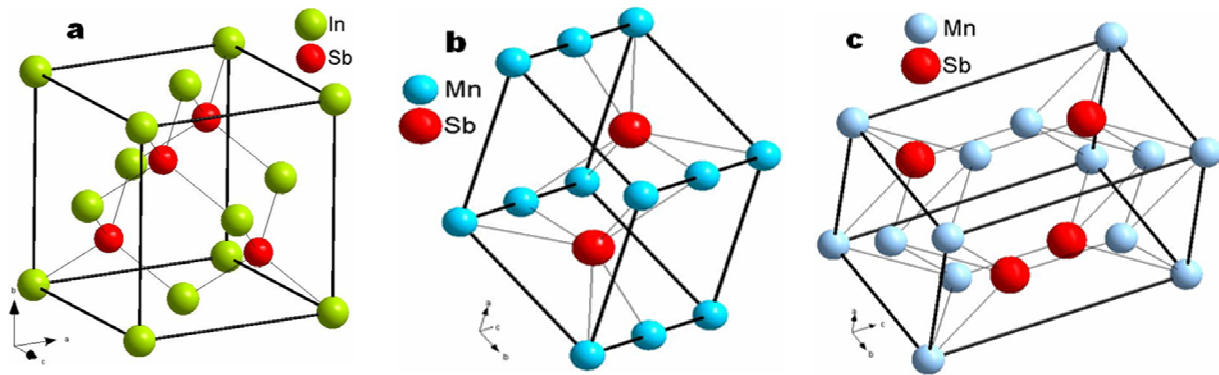


Fig. 1. Elementary unit cells of $InSb$ (a), $MnSb$ (b) and Mn_2Sb (c) compounds

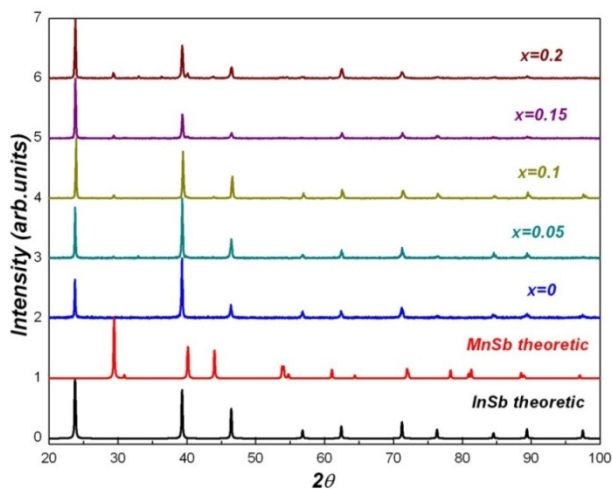


Fig. 2. X-ray diffraction patterns of $In_{1-x}Sb_xMn_x$ system

After preparation the quality and crystallographic structure of investigated sample was checked by means of X-ray diffraction. The corresponding XRD patterns are shown in Fig. 2. XRD patterns indicate the existence of an $InSb$ structure type phase and also the presence of some small $MnSb$ peaks. The ferrimagnetic Mn_2Sb phase is not visible due to diffractometer resolution. The presence of both $MnSb$ and Mn_2Sb phases could be pointed out only by using synchrotron radiation, as

previously shown by *Novotortsev et al.* study [31] on bulk material, in the $0.01 \leq x \leq 0.06$ concentration range. From the most intense *MnSb* line recorded by *XRD* measurements and using *Scherrer's equation* [35]

$$d = \frac{0.9\lambda}{\beta \cos\theta}$$

where λ represents the X-ray wavelength, β is the angular width at half-maximum intensity and θ the diffraction angle, it is possible to estimate the diameter d of the magnetic particles.

3.1.2. TEM analysis

TEM images show the presence of some manganese antimonide phase microinclusions (the darker particle centres) imbedded in the semiconductor *InSb* matrix (light coloured coating). The dimensions of these clusters are between (30-40) nm, in good agreement with those obtained from *XRD* patterns, using Scherrer's equation. But these measurements did not allow us to identify the exact composition of the clusters. The microinclusions might be identified as either *MnSb* or *Mn₂Sb*.

3.1.3. Magnetic measurements

Earlier studies of *Novotortsev et al.* [31] on bulk *In_{1-x}Mn_xSb*, performed in the $x = (0.01-0.06)$ % *Mn* concentration range, pointed out the presence in the investigated samples of *In_{1-x}Mn_xSb* ferromagnetic solid solution with $T_C < 10K$ together with two additional manganese antimonide phase microinclusions: ferromagnetic *MnSb* and ferrimagnetic *Mn₂Sb*. Our aim was to observe and study the magnetic behaviour in case of this system, for concentrations that go beyond the solid solubility limit. For this purpose several magnetic measurements were performed. Magnetic susceptibility at low magnetic field ($B=0.01T$) was carried out on a superconducting quantum interference device (*SQUID* magnetometer) from 2 to 300K. The variation of the magnetization with temperature at 0.2T and 0.8T magnetic field was measured using a *Weiss* balance in the (300-700)K temperature range. The hysteresis loop at $T=5K$ was recorded using an *OXFORD* device.

MnSb has a magnetic moment of $3.3-3.5 \mu_B$ on *Mn* sites, and $-0.06 \mu_B$ on *Sb* site [32, 33]. In the tetragonal unit cell of *Mn₂Sb*, there are two crystallographically non-equivalent sites for *Mn* atoms, *Mn(I)* ($2.1 \mu_B$) and *Mn(II)* ($3.9 \mu_B$) aligned antiparallel to each other [34] resulting a mean value of $0.9 \mu_B$ per *Mn* atom.

At higher fields (0.8T) (**Fig. 4a**) the alloys seem to show a ferromagnetism with the *Curie* temperature T_C in the (550-590)K range, determined from the $M^2(T)$ plot in the molecular field approximation. The *Curie* temperature values are situated between the *Curie* temperature of ferromagnetic *MnSb* ($T_c \sim 585K$) and ferrimagnetic *Mn₂Sb* ($T_c \sim 550K$) [36] compounds. The temperature dependence of the magnetization for these two compounds is given in **Fig. 4c**. The magnetizations plots $M(T)$ for $B=0.8T$ (**Fig. 4a**) present a deviation from the normal Brillouin curve in the (400-500)K temperature range. This anomaly may be due to the mediated contribution of *MnSb* and *Mn₂Sb* clusters. Both magnetization and *Curie* temperature decrease with decreasing *Mn* concentration.

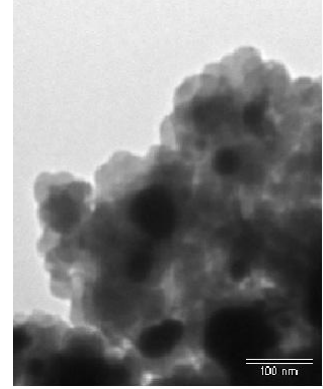
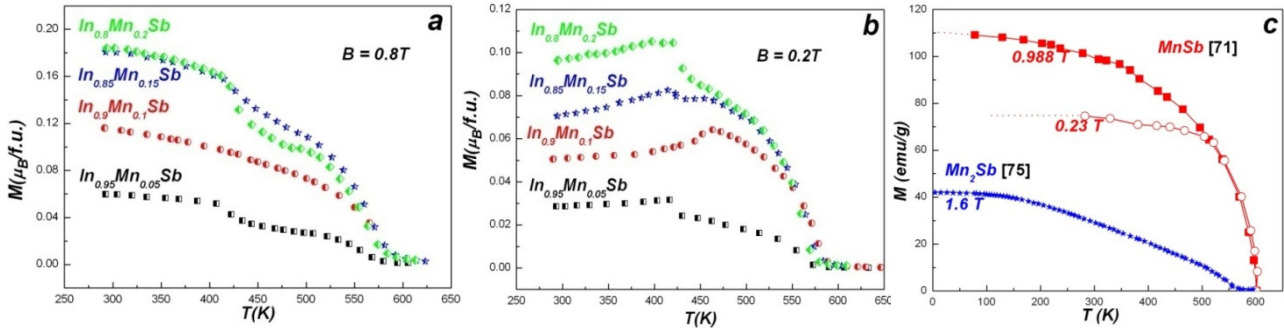


Fig. 3. Imagine TEM a probei *In_{0.9}Mn_{0.1}Sb*

In lower magnetic field ($0.2T$), however, the magnetizations versus temperature curves show a broad maximum around $425K$. This type of maximum in the $M(T)$ curves is sometimes observed in micromagnetism or cluster spin glass owing to the coexistence of ferromagnetic and antiferromagnetic interactions. The exchange interactions between the ferromagnetic and ferrimagnetic entities, at their interfaces, leads to different configurationally “pinning” [37] of ferromagnetic components.

The increase of the magnetization with temperature for small magnetic fields (**Fig. 4b.**) suggests that up to a certain temperature the influence of the ferrimagnetic component on the magnetization of



$MnSb$ clusters is more pronounced for smaller magnetic field.

Fig. 4. Magnetization as a function of temperature for $In_{1-x}Mn_xSb$ system at $0.8 T$ (a) and $0.2 T$ (b), $MnSb$ and Mn_2Sb compounds (c)

When Mn_2Sb is modified with Cr , resulting in the compounds $Mn_{2-x}Cr_xSb$ ($0.01 < x < 0.25$), a magnetic phase transition at temperature T_S is induced. This transition is from ferrimagnetic above T_S , to antiferromagnetic below T_S : T_S increases with increasing Cr content. At the phase transition there is a discontinuous decrease of the c axis and increase of a axis. The transition takes place at the critical value of 6.53\AA corresponding to the c axis, for every Cr content [38]. *Kittel* has shown that such first-order magnetic transformation can occur when the magnetic exchange interaction is coupled with the lattice elastic strain, and when the net exchange is zero for the some critical value of the lattice parameter, that is attainable by temperature variation. The role of Cr substitution for Mn in the $Mn_{2-x}Cr_xSb$ system is to contract the Mn_2Sb lattice, so that the critical dimension is thermally achieved.

At the $Mn_2Sb/MnSb$ interface, an antiferromagnetic layer can develop in Mn_2Sb , due to the contraction of c lattice parameter, caused by the lattice constants mismatch of the two compounds. The ferromagnetic $MnSb$, which is strongly coupled with the antiferromagnetic layer from Mn_2Sb , has its interfacial spins pinned. All these results suggest the coexistence of ferromagnetic $MnSb$ and ferrimagnetic Mn_2Sb clusters in the $In_{1-x}Mn_xSb$ alloys.

The formation of manganese antimonide clusters in the investigated alloys is also suggested by the hysteresis loop measurements. The field dependence of the magnetization for $In_{0.9}Mn_{0.1}Sb$ is shown in **Fig.5**. Similar curves were obtained in case of all investigated alloys. The saturation magnetisation is observed in fields higher than $0.5T$.

The magnetization in the very small field region (**Fig. 3.5b**) shows that for all investigated materials the coercitive field is very small (does not exceed $20 Gs$). This characteristic is typical

for clusters behaviour. The small values of the coercitive field and saturation field may be explained in the random anisotropy model [39]. Furthermore, the hysteresis loop shows a small asymmetry with a shift towards negative field. This is due to the exchange interaction between the ferromagnetic and ferrimagnetic phase at their interface. Such exchange bias fields have been observed in case of many ferromagnet/ferrimagnet interfaces like $\gamma\text{-Fe}_2\text{O}_3/\text{Fe}$ [37] and Co/TbFe [40].

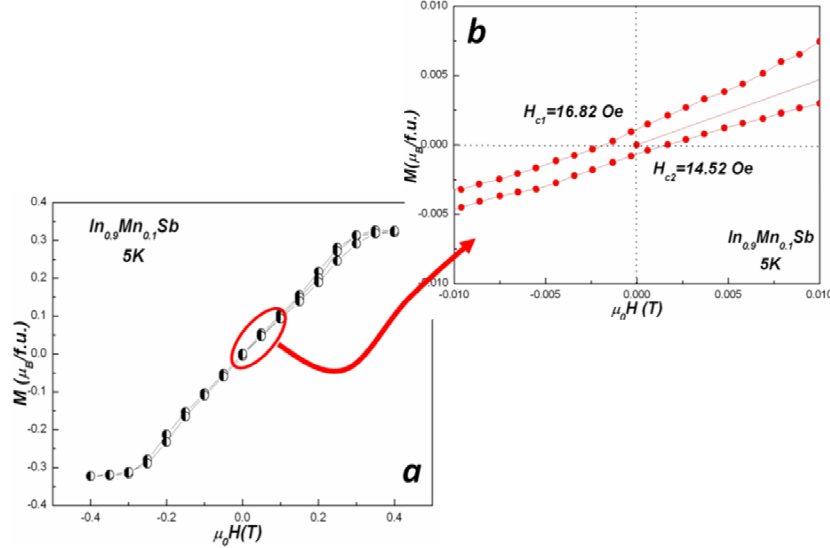


Fig. 5. Hysteresis loop performed at 5K (a) and magnetization in the very small field region (b) of $\text{In}_{0.9}\text{Mn}_{0.1}\text{Sb}$ compound

The values of magnetic moment per manganese atom in $\text{In}_{1-x}\text{Mn}_x\text{Sb}$ alloys (for $x \leq 0.2$), determined from saturation magnetisation at $T=5\text{K}$, are in the $(2.07\text{-}3.28)\mu_B$ range (**Table 1**).

Tabelul 1. Magnetic moment per Mn atom determined from magnetic measurements performed at $T=5\text{K}$

Manganese concentration (% at.)	0.05	0.1	0.15	0.2
Magnetic moment per Mn atom (μ_B)	3	3.28	3.1	2.07

The obtained values are in good agreement with earlier studies in the $x = (0.01\text{-}0.06)$ % Mn concentration range [31]. The substitution of *In* by *Mn* brings no significant changes in the *Mn* 3d band. For higher *Mn* concentrations ($x > 0.15$),

the magnetic moment per *Mn* atom decreases, suggesting the increasement of ferrimagnetic contribution provided by Mn_2Sb clusters.

Magnetic measurements in much lower fields ($B=0.01\text{T}$) also reveal the coexistence of two types of magnetic clusters Mn_2Sb and MnSb . The temperature dependence of the field cooled (FC) and zero field cooled (ZFC) magnetic susceptibility were recorded with a SQUID magnetometer (*Superconducting Quantum Interference Device*), in France, at “*Institut des Matériaux Jean Rouxel*”, *Université de Nantes*. The temperature dependence of FC and ZFC magnetic susceptibility for $\text{In}_{0.8}\text{Mn}_{0.2}\text{Sb}$ and $\text{In}_{0.95}\text{Mn}_{0.05}\text{Sb}$ alloys are given in **Fig. 6**. Magnetic susceptibility measured with SQUID magnetometer (lines) and Weiss magnetic balance (lines and circles) for $\text{In}_{0.8}\text{Mn}_{0.2}\text{Sb}$ is given in **Fig. 6a**.

In the inset of **Fig. 6a** the temperature dependence of the crystalline anisotropy energy coefficients K_1 for Mn_2Sb compound is given. At temperatures below $240K$ the magnetic moments in Mn_2Sb are directed perpendicular to the c axis. At $240K$ the anisotropy changes sign and above this temperature the easy axis of magnetization is parallel to the c axis [38].

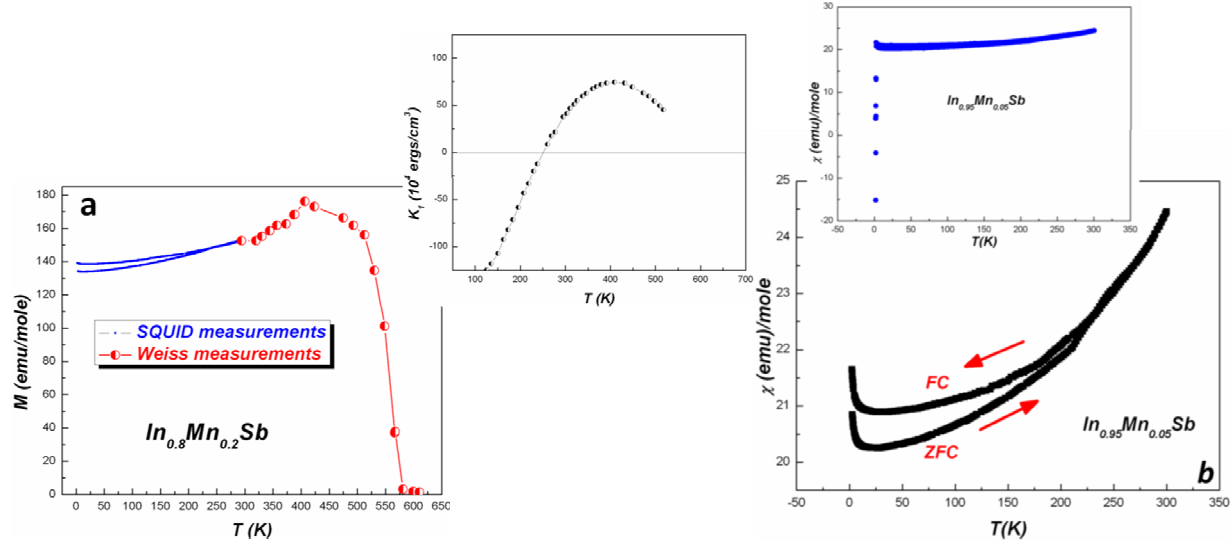


Fig. 6. FC and ZFC magnetic susceptibility versus temperature of $In_{0.8}Mn_{0.2}Sb$ (a) and $In_{0.95}Mn_{0.05}Sb$ (b) at $B=0.01T$

The temperature dependence of field cooled (FC) and zero field cooled (ZFC) magnetic susceptibility of $In_{0.95}Mn_{0.05}Sb$ alloy, at small fields ($B=0.01T$) is shown in **Fig. 6b**. Similar curves were obtained for all investigated alloys.

A dominant feature is the splitting between FC and the ZFC susceptibility which confirms the coexistence of two types of magnetic microinclusions: ferrimagnetic Mn_2Sb clusters and ferromagnetic $MnSb$ clusters.

It is interesting to note that the splitting of FC and ZFC susceptibility takes place, for all investigated alloys, at the same temperature where the anisotropy coefficient K_1 changes its sign, so that the anisotropy energy is negligible in comparison with the exchange energy.

The mixed state incorporates ferromagnetic and ferrimagnetic parts for which close-lying Curie temperature T_C were identified from magnetization measurements. As a consequence of the mixed magnetic interactions, in these alloys there is pinning of the ferromagnetic parts caused by the ferrimagnetic environment, as evidenced also by the splitting in the FC and ZFC magnetic susceptibility measurements.

The susceptibility versus temperature exhibits a magnetic field cooling effect below the freezing temperature $T_f \sim 240K$. For all alloys a maximum in $\chi(T)$ is observed between the Curie temperature and $240K$, the latter corresponding to the onset of mictomagnetism or cluster spin glass. A similar behaviour was observed in many mictomagnetic systems such as the ϵ phase of the $Mn-Zn$ alloy system [41]. The upward of the magnetic susceptibilities at very low temperatures (**Fig. 6b.**) is due to the ferromagnetic phase formation in the $In_{1-x}Mn_xSb$ solid solution.

For small manganese concentration ($x=0.05$) a superconductor behaviour can be observed in the low temperature region due to some indium segregated particles (Indium $T_c=3.4K$ [42]) - the inset of Fig.6b.

3.1.4. XPS spectra

The electronic structure of investigated alloys is studied by means of *X-Ray Photoelectron Spectroscopy*, analyzing the valence band and core level spectra. The surface cleanness was checked by monitoring the *O 1s* and *C 1s* core levels in the survey spectra.

Valence band spectra

The XPS valence band spectra of $In_{1-x}Mn_xSb$ alloys are shown in Fig. 7, comparative with $MnSb$ and Mn_2Sb compounds.

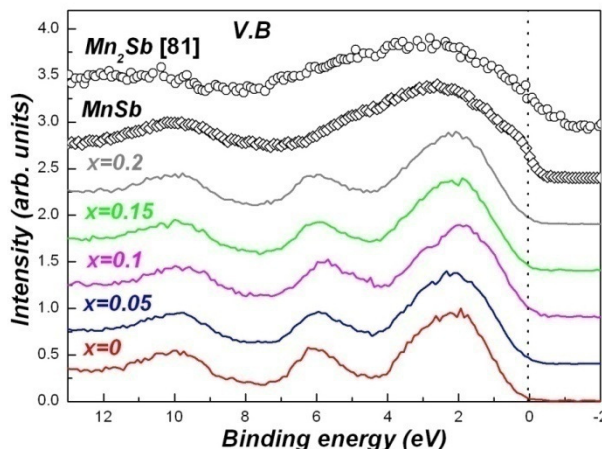


Fig.7 . Comparison between XPS valence band spectra of $In_{1-x}Mn_xSb$ alloys, $MnSb$ and Mn_2Sb compounds

The XPS valence band spectra were calculated with the *Munich SPR-KKR package* [22] (Fig. 8a).

One can observe that for both compounds the *Mn 3d* contribution to the valence band has a maximum around $2.8 eV$, which is also reflected in the valence band spectra of $In_{1-x}Mn_xSb$ alloys. The computed XPS valence band spectrum of $MnSb$ is in good agreement with the experimental results, indicating that the measured spectrum is representative of the bulk.

For $Al K\alpha$ radiation, the *In* and *Sb* cross sections are comparable, as a consequence, the valence band spectra are being dominated by *In 5p* and *Sb 5p* contributions. The density of states (*DOS*) at Fermi level increases with *Mn* content. The half width at half maximum (*HWHM*) also increases, suggesting the increase of *Mn 3d* contribution around $2.8 eV$. The spectral structure which appears around $10-11 eV$ is characteristic for *Sb 5s* levels.

A better understanding of the main characteristics in the valence band requires a comparison between the experimental and the

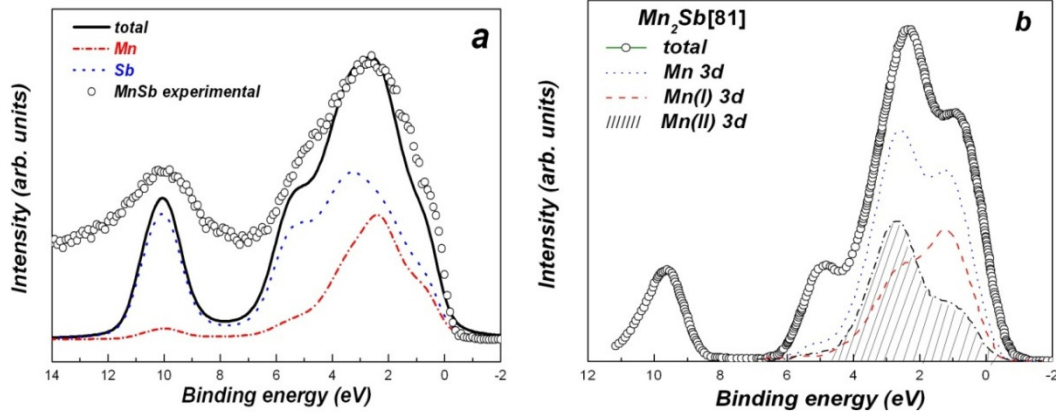


Fig. 8. Calculated (lines) and experimental (circles) XPS valence band spectra of *MnSb*(a) and calculated total and partial DOS of ferromagnetic *Mn₂Sb* compound (b)

Core-level XPS spectra

Mn 2p core level XPS spectra

The Mn 2p core level spectra are presented in **Fig. 9**, together with *MnSb* and *Mn₂Sb* corresponding spectra. The XPS peaks associated to these levels could be recorded only for high manganese concentration ($x=0.15$ and $x=0.2$) due to the spectrometer resolution.

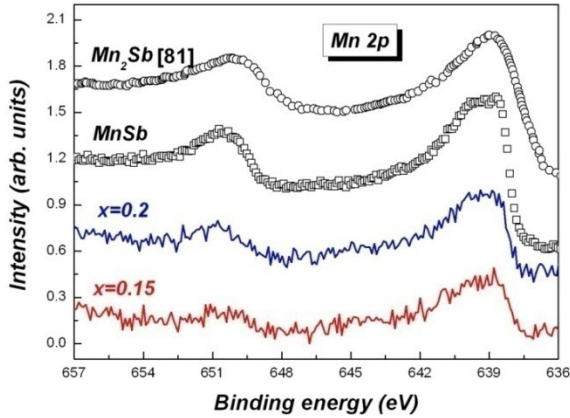


Fig. 9. XPS Mn 2p core level spectra of *In_{0.85}Mn_{0.15}Sb*, *In_{0.8}Mn_{0.2}Sb*, *MnSb* and *Mn₂Sb*

Mn 2p XPS spectra of *In_{1-x}Mn_xSb* ($x=0.15$ and 0.2) present a spin-orbit splitting of ~ 11 eV, which can be identified in the distance between the energy centres of the $2p_{3/2}$ and $2p_{1/2}$ states. In case of atomic *Mn*, experimental and theoretical results revealed a fine structure of the $2p$ photoelectron spectrum caused by the Coulomb interactions of the $2p$ hole and $3d$ valence electrons. The line shapes of $2p$ core-level photoemission spectra for $3d$ metals are strongly influenced by the simultaneous occurrence of spin-orbit coupling and exchange splitting between the core hole and valence electrons. The theoretical approach to the problem of core-level photoemission is done within

a fully relativistic generalization of the one-step model of photoemission. *Ebert et al.* found in the calculated spectra a splitting of $2p_{3/2}$ and $2p_{1/2}$ states into four and respectively two sublevels [43]. Using the fully relativistic photoemission calculations *Plogman et al.* found a splitting of the *Mn 2p_{3/2}* states into four sublevels [44]. This gives direct evidence of the existence of local moments in the *Anderson's* sense confined on *Mn* sites [11].

Fig. 10. shows the fitting of *Mn 2p_{3/2}* XPS spectra for *MnSb*, *In_{0.85}Mn_{0.15}Sb* and *In_{0.8}Mn_{0.2}Sb*. The fitting results were obtained considering four components and a satellite line just like in all other alloys and intermetallic compounds based on *Mn* [43-45].

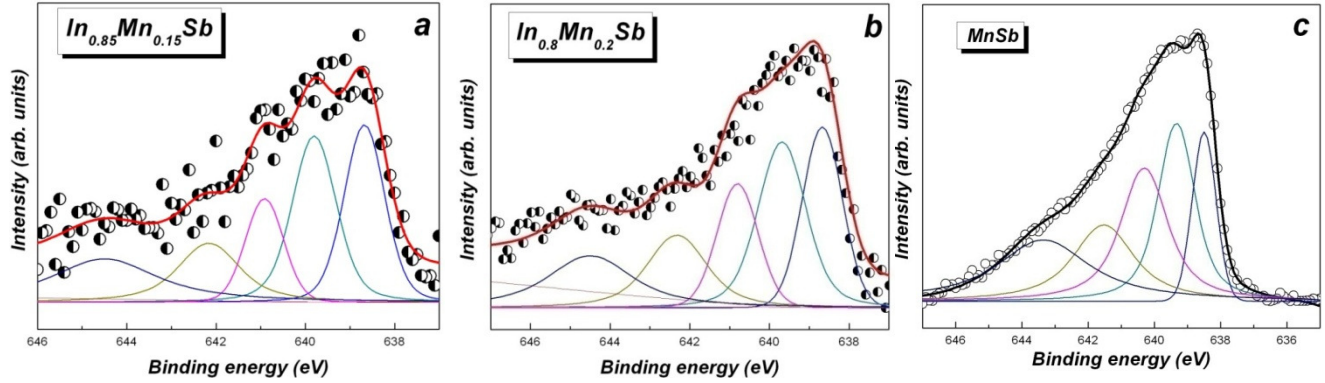


Fig.10. Curve fitting results (solid lines) of Mn $2p_{3/2}$ core level spectra of MnSb (a) and $In_{0.8}Mn_{0.2}Sb$ alloy (b) superposed on the measured spectra (circles)

The full width at half maximum (*FWHM*) of each multiplet peak was considered between 1 eV and 1.5 eV, with a 0.4eV Lorentian contribution (accounting the Mn 2p hole states lifetime [46]) and a 0.6-0.8 eV Gaussian contribution (accounting for the instrumental broadening). The relative intensities of these states vary depending on Mn atomic environment, reflecting the changes induced to the properties of Mn 3d states. The binding energies of the fitted multiplet splitting components and the mean energy separation between the four components, which corresponds to the exchange splitting of the Mn $2p_{3/2}$ core-hole states, are listed in the next table (Table 2). The Mn 2p core level spectra for $x=0.15$ and $x=0.2$ resemble those of MnSb and Mn_2Sb intermetallic compounds. The mean exchange splitting in the investigated alloys are very close to that found in MnSb compound and confirm the existence of local magnetic moments confined on Mn sites.

Table 2. Fitting parameters for Mn $2p_{3/2}$ XPS spectra of $In_{1-x}Mn_xSb$ ($x= 0.15$ and 0.2) alloy and MnSb compound. Δ_{ex} denotes the mean exchange splitting between the sublevels

x	Binding energy (eV)				
	Component 1	Component 2	Component 3	Component 4	Δ_{ex} (eV)
0	638.5	639.3	640.3	641.5	1.01
0.15	638.7	639.8	640.9	642.2	1.16
0.2	638.6	639.6	640.7	642.2	1.2

Sb 3d core level XPS spectra

Due to spin-orbit splitting the Sb 3d spectrum consists from two components: $3d_{3/2}$ and $3d_{5/2}$. In analysed compounds the splitting between these two centres is around 9.4eV, comparable to that in pure Sb. The lack of O 1s at 531eV binding energy in the Sb 3d core level spectra indicates that contamination is absent and proves the good quality of the investigated sample A

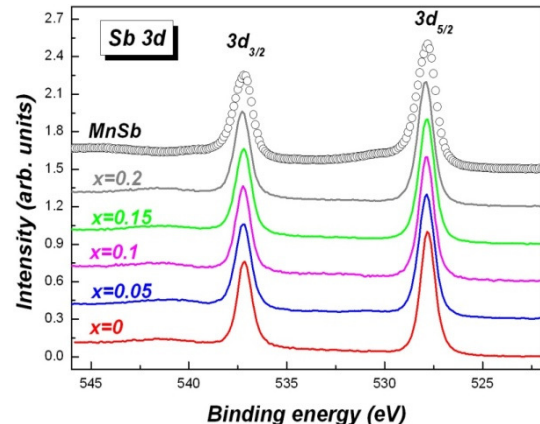


Fig. 11. XPS Sb 3d core level spectra of

$In_{1-x}Mn_xSb$ system together with MnSb Sb 3d

strong interaction exists between *Mn-Mn* and *Mn-Sb*; the corresponding coupling can be described in terms of covalent interaction between unoccupied *Sb 5p* states and *Mn 3d* band.

3.1.4. Summary

The substitution of *In* by *Mn* in *InSb* beyond the solid solubility limit leads to the formation of magnetic clusters. Magnetic measurements performed at high and small magnetic field, *FC* and *ZFC* measurements, on *In_{1-x}Mn_xSb* ($x=0.05, 0.1, 0.15$ and 0.2) system indicates the coexistence of two types of magnetic clusters: ferromagnetic *MnSb* and also ferrimagnetic *Mn₂Sb*. *TEM* images also show some manganese antimonide phase microinclusions with dimension between (30-40) *nm*. *XPS* valence band and *Mn 2p* core level spectra have confirmed the presence of manganese antimonide phases. The substitution of *In* by *Mn* brings no significant changes in the *Mn 3d* band. For higher *Mn* concentrations ($x>0.15$), the magnetic moment per *Mn* atom decreases, suggesting the increasement of ferrimagnetic contribution provided by *Mn₂Sb* clusters.

3.2. Magnetic cluster development in oxidized *CeNi₅* powder [47, 48]

Nanosized particles of ferromagnetic metals (*Fe*, *Co*, *Ni*) have been widely studied as they present an interest both for fundamental physics and potential applications such as catalysis, high density magnetic recording media, ferrofluids and medical diagnostics. However, synthesis, handling and storage of such materials give rise to problems related both to their size control and to the stabilization of the highly reactive resulting product. Several methods have been used for the production of such particles: evaporation [49-52], sputtering [53], and various chemical methods [35, 54, 55]. Evaporation techniques allow producing isolated particles whereas the others are used to produce particles dispersed in an insulating matrix.

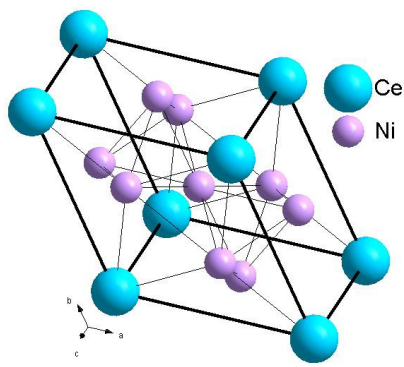
Magnetic nanoparticles covered with a layer of antiferromagnetic oxide exhibit the exchange anisotropy phenomena, with potential technological application [56] if an antiferromagnetic coating materials with a *Néel* temperature above room temperature can be produced (e.g. $T_N=525K$ for *NiO*).

Rare earth oxides are potentially useful materials for various optical and electronic applications. One such material is cerium dioxide (*CeO₂*) due to his high refractive index (~2), high transparency in the visible and near-infrared region and large dielectric constant (~26) [57].

In case of *CeNi₅* previous magnetic studies have shown that *Ce* atoms are in an intermediary valence state. The *Ni-Ni* distances are very close to those from pure metallic *Ni*, fact that determines a strong interaction between *Ni* atoms. Taking into account the great oxygen affinity of *Ce* and the strong magnetic interactions between *Ni* atoms in this compound, we tried to obtain *Ni* metallic clusters covered by *NiO*, *Ce₂O₃* and *CeO₂* by mechanically transforming the bulk *CeNi₅* in a very fine powder followed by a thermal treatment in air at different temperatures up to 800°C.

3.2.1. Synthesis and structural characterisation

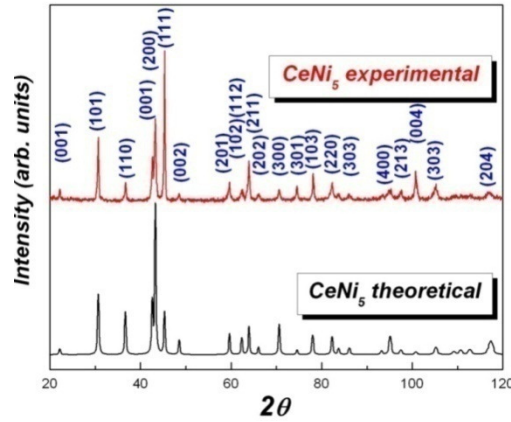
The starting material *CeNi₅* was prepared by argon arc melting method. The purity of starting materials was 99.9% for both *Ce* and *Ni*. The *CeNi₅* compound crystallizes in the hexagonal



$CaCu_5$ structure type, space group $P6/mmm$ with Ce occupying the $1a$ site $(0, 0, 0)$, $Ni(1)$ in the $2c$ site $(1/3, 2/3, 0)$ and $Ni(2)$ in the $3g$ sites $(1/2, 0, 1/2)$ (**Fig. 12.**). The $Ni-Ni$ distances in $CeNi_5$ are $0.244nm$ very close to those of pure metallic Ni , $0.249nm$, respectively [58].

Fig. 12. The $CeNi_5$ unit cell

This enhanced Pauli intermediate showed that the all peaks can be lines of expected lattice parameters



compound is an exchange-paramagnet and Ce ions are in the valence state [59, 60]. XRD pattern initial compound is single phase and indexed according the characteristic structure type with the following $a = 0.487nm$ and $c = 0.402nm$ in

Fig. 13. Spectrul XRD teoretic și experimental al compusului $CeNi_5$

good agreement with earlier findings [58].

The crystallite size of initial $CeNi_5$ compound was calculated from the (002) profile of XRD pattern. Generally it is not easy to obtain accurate values of the crystallite size without extreme care in the experimental measurements and analysis of diffraction data. XRD line profile analysis is a versatile nondestructive method that can be used in obtaining nanostructural information. Usually the nano-crystallite size is determined by classical Scherrer equation [35]. For a better accuracy in the determination of full width at half maximum (FWHM) of the X-Ray line profile (XRLP) approximation methods like Cauchy [61], Gauss [62], Voigt [63] or Generalized Fermi Function (GFF) [64] are used.

The same four methods were adopted in the approximation of $CeNi_5$ XRLP. The doublet correction $K\alpha_2$ was realized by the installation soft. The background approximation was necessary in order to obtain a correct value of the FWHM; this approximation was realised using a regression line defined on the two XRD lobes.

Table 3. Global structural parameters of initial compound $CeNi_5$

	Gauss	Cauchy	Voigt	GFF
d(nm)	30.6	40.9	45.4	34.7
FWHM($2\theta^\circ$)	0.33	0.23	0.27	0.27
χ^2	997	903	864	839

χ^2 is the root squares of residuals. In case of initial compound $CeNi_5$ the FWHM was calculated using the

Scherrer's equation from the GFF approximation results for which we have a minimum value of the root squares of residuals. The average crystallite size of the starting material was about $34.7nm$. In order to evaluate which approximation method gives the best results in the fitting of experimental XRLP, an additional parameter χ (goodness of the fit) was introduced:

$$\chi(\%) = \sqrt{\frac{\sum_{i=1}^{N_p} [(I)_{obs}(2\theta_i) - I_{calc}(2\theta_i)]^2}{(N_p - N_{par}) \sum_{i=1}^{N_p} I_{obs}^2(2\theta_i)}} \cdot 100, \text{ where: } \chi^2 = \sqrt{\frac{\sum_{i=1}^{N_p} [(I)_{obs}(2\theta_i) - I_{calc}(2\theta_i)]^2}{N_p - N_{par}}}$$

I_{obs} represents the intensity of experimental XRD pattern, I_{calc} is the calculated intensity, N_p is the number of considered experimental points and N_{par} refers to freedom degrees, which is a specific parameter for each approximation method. The goodness of the fit expresses the difference between the experimental and calculated results. From the numerical analysis of XRLP it is known that in case of a satisfactory fit, χ has values up to 5% [65]. Goodness of the fit, in case of initial $CeNi_5$ was 2.08%.

After heat treatment, in order to determine crystalline structure, each sample was investigated through mean of XRD method (Fig. 14.).

We have observed that crushed $CeNi_5$ becomes magnetic upon exposure to air for 40 min. at 100 °C. It is well known that Ce is much more sensitive to oxygen than Ni, this result suggest that Ni atoms diffuse into particles to form magnetic clusters, due to the strong magnetic interactions between the nearest - neighbours Ni atoms, and Ce ions migrate to the surface of the particles during heat treatment to form the oxide layers of CeO_2 and Ce_2O_3 .

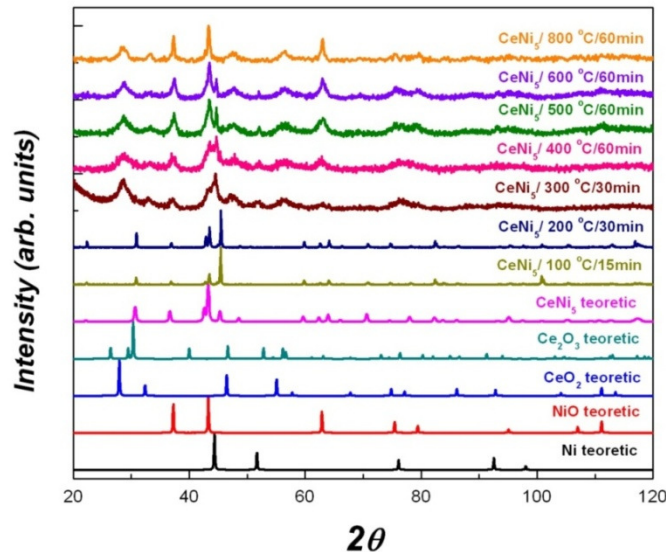


Fig. 14. XRD patterns for $CeNi_5$ oxidized in air at different temperatures and theoretical patterns corresponding to pure metallic Ni, NiO, CeO_2 , Ce_2O_3 and $CeNi_5$

A major advantage is represented by the fact that, at high temperatures, a thin NiO layer appears, resulting a Ni/NiO (ferromagnet/antiferromagnet), which determines exchange anisotropy. The Ce oxide layers and, in a very small quantity, NiO formed on the surface of Ni particles are not continuous and consist of very small crystallites. The surface of Ni particles is completely oxidized after a new heating for 1 h at 600 °C, and only NiO and CeO_2 layers can be detected

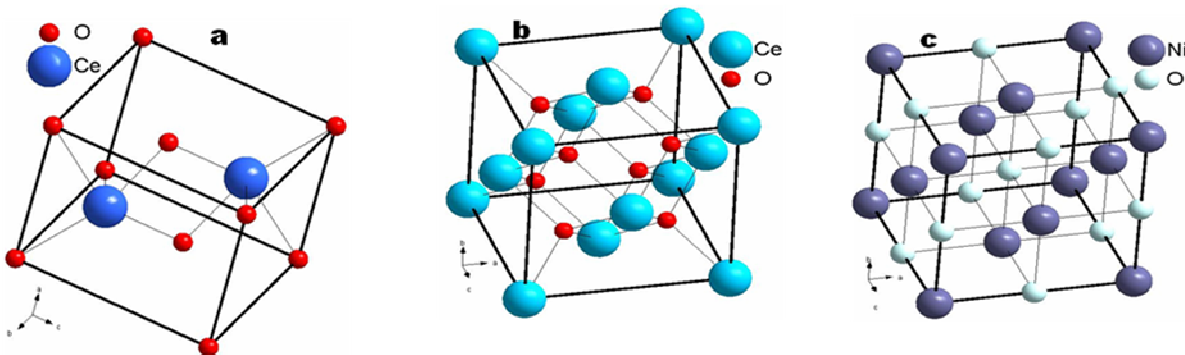


Fig. 15. Elementary unit cells of Ce and Ni oxides: Ce_2O_3 (a), CeO_2 (b) and NiO (c)

For some of the treated samples ($CeNi_5$ oxidized in air at $300^\circ C$, $400^\circ C$, $500^\circ C$ and $600^\circ C$) the Ni (200) and NiO (110) X-Ray diffraction profiles were processed in order to evaluate the average crystalline size of Ni core and NiO layer formed on Ni particles surface. The same four methods (*Cauchy*, *Gauss*, *Voigt* and *GFF*) were adopted in the approximation of *XRLP*.

The crystalline average size of Ni clusters increases with temperature due to recrystallization processes that occur during the heat treatment from $34nm$ to $77nm$. These values were determined from *Scherrer* equation, based on *Voigt* approximation results, for which we have obtained a minimum value of χ^2 . In case of Ni metallic cores the obtained values for χ (goodness of the fit) are between 1.26 - 3.34 %. The thickness of NiO layer also increases with temperature, from $9nm$, in case of $CeNi_5$ oxidized in air at $300^\circ C$ for 30 min, up to $19nm$, for $CeNi_5$ treated at $600^\circ C$ for one hour. These values were determined using *Scherrer's* equation applied to *Voigt* approximation results, for which χ^2 has its minimum value. The associated goodness of the fit for these approximations has values in the 2.4 - 2.65 % range.

3.2.2. TEM analysis

TEM image (Fig. 16.) shows the presence of darker particle centres surrounded by a light colour coating in most of the particles. This could be attributed to a core-shell type of structure, where the core consists of metallic cores. The mean Ni particle diameters are in good agreement with those obtained from *XRD* measurements.

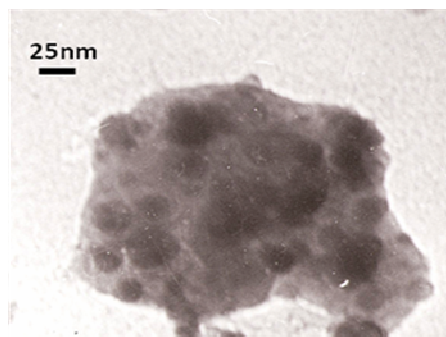


Fig. 16. TEM image of $CeNi_5$ powder oxidized in air at $800^\circ C$ for 1h

3.2.3. Magnetic measurements

The magnetic properties of exchange-enhanced *Pauli* paramagnet $CeNi_5$ have been extensively studied for many years; however, the magnetic behaviour of this compound at finite temperatures is not well understood. Magnetic measurements have shown a thermal variation of the magnetic susceptibility in a large temperature range. The magnetic susceptibility and reciprocal susceptibility versus temperature for $CeNi_5$ are shown in Fig. 17. The measurements were performed using Weiss balance in the 80 - 800 K temperature range.

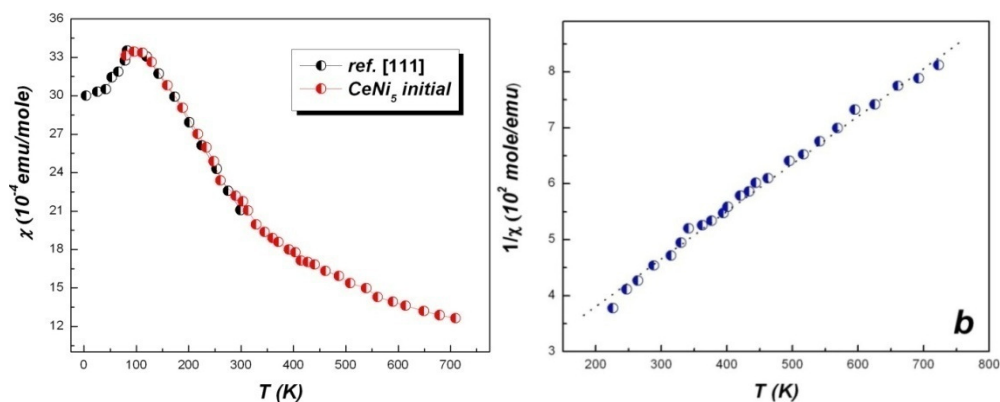


Fig. 17. Thermal variation of the susceptibility (a) and of the reciprocal (b)

susceptibility (b) for $CeNi_5$.

The experimental curve obtained in case of susceptibility thermal variation is in good agreement with previous measurements of *Grignoux et al.* in the 1.4 - 300 K temperature range [66].

The $CeNi_5$ susceptibility arises mainly from the $Ni\ 3d$ electrons which are close to the onset of ferromagnetism. The $Ni\ 3d$ band is partially empty but does not show magnetic splitting. In this compound Ce is in an intermediary valence state close to $4+$, this means that it brings no contribution to the magnetic moment. Therefore, in this case we have to deal with spin fluctuation suggested by the apparition of some induced magnetic moments at Ni position. The average amplitude of longitudinal local spin fluctuations increases with temperature until it reaches an upper limit. The temperature dependence of χ at low temperature is the result of the increase in local moments with increasing temperature. The amplitude of thermally excited longitudinal spin fluctuations saturates at a certain temperature, above which the susceptibility is governed by local moment type fluctuations and therefore a *Curie-Weiss* law modified by a temperature-independent part χ_0 is observed: $\chi = C(T - \theta) + \chi_0$.

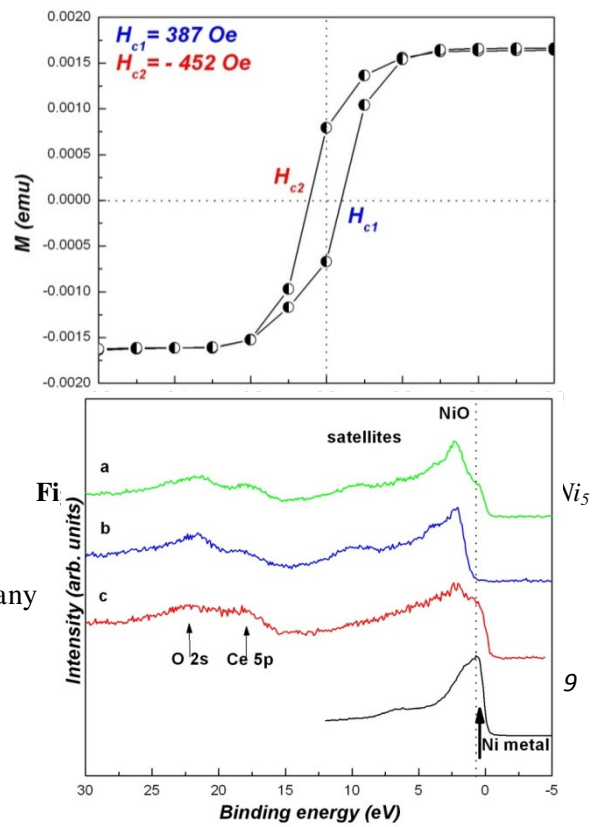
For temperatures smaller than the critical value ($T_c=100K$), the magnetic susceptibility of $CeNi_5$ shows much higher values than those obtained in the free electron approximation. We have to deal with a *Pauli* exchange-enhanced paramagnet, which implies the existence of some strong correlation between $Ni\ 3d$ electrons.

The paramagnetic *Curie* temperature is negative and very large $\theta = -275K$, and the effective magnetic moment per Ni atoms, determined from the *Curie* constant, is $1.34\ \mu_B$.

The $1/\chi(T)$ curve present a deviation from linearity around $T^* \sim 330\ K$, in accord with the predictions of self-consistent renormalization theory (*SCR*) of spin fluctuation [118]. In the $T < T^*$ region, $CeNi_5$ shows an exchange-enhanced *Pauli* paramagnetism, and the apparition of temperature induced local moments is very rapid.

The maximum of the bulk susceptibility in $CeNi_5$ corresponds to a maximum of Ni atoms susceptibility in this compound. A partial spin fluctuation quenching appears due to $4f-5d$ and $3d-5d$ hybridizations.

The hysteresis loop of $CeNi_5$ powder oxidized in air at $600^\circ C$ for one hour (**Fig. 18.**) pointed out the phenomena of exchange anisotropy as a result of interactions between antiferromagnetic NiO layer and ferromagnetic Ni core. The hysteresis was measured after the sample was cooled from room temperature to $5K$ in an applied field of $1T$. One can see a small asymmetry of the hysteresis loop, with a shift towards negative magnetic field. This is due to the exchange interaction between the ferromagnetic and antiferromagnetic phase at their interface. Such exchange bias fields have been observed in case of many



ferromagnet/antiferromagnet[68, 69]or ferromagnet/ferrimagnet interfaces [26, 37].

3.2.4. XPS spectra

The surface response of fine $CeNi_5$ particles upon oxidation has been studied by following the modification of XPS valence band, $Ni\ 2p$ and $Ce\ 3d$ core levels with heat treatment temperature and time. Furthermore, the as – prepared samples were sputtered using an argon ion beam and a surface profile depth was performed.

Valence band spectra

The valence bands of $CeNi_5$ powder, oxidized in air at $300^\circ C$ for 30 min and $600^\circ C$ for an hour, before and after 10 min and 17 min argon etching are shown in Fig. 19.

After sputtering, the apparition of a new feature located in the low energy region of the spectra, near the Fermi level, is evident. This new feature is attributed to $3d$ states of pure metallic Ni situated at about $0.6eV$. The Ni component is evident only after the removal of surface NiO layer, during the sputtering process, and confirms the formation of Ni metallic cluster.

Core-level XPS spectra

$Ni\ 2p$ and $Ce\ 3d$ core level XPS spectra

The main characteristic of $Ce\ 3d$ levels is the spin-orbit splitting of $\sim 18\ eV$, between $Ce\ 3d_{3/2}$ and $Ce\ 3d_{5/2}$ centres [70] (Fig. 20.) which lead to the apparition of six components instead of three ones predicted by theoretical calculations [71-73]. These measurements suggest the existence of an intermediary valence state at Ce position, and the fact that $3d^0f^0$ and $3d^0f^2$ are overlapped.

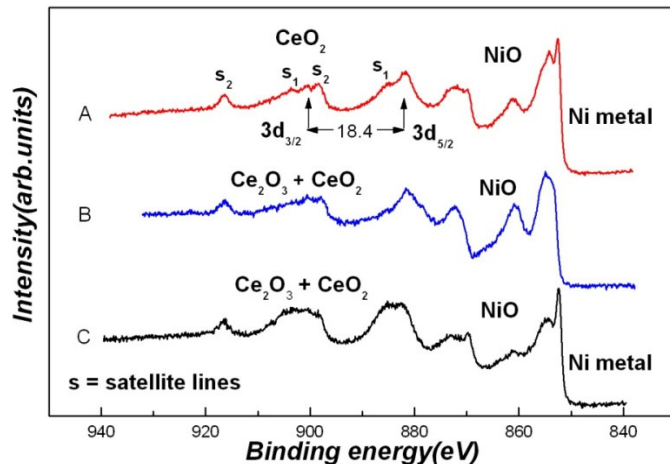
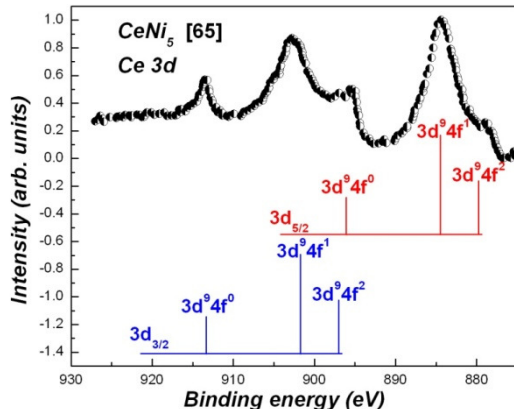


Fig. 19. XPS valence band spectra of $CeNi_5$ powder oxidized in air at $600^\circ C$ for 1h and exposure time to ion etching $\tau = 10\ min$. (a), oxidized in air at $600^\circ C$ for 1h without sputtering (b) and oxidized in air at $300^\circ C$ for 30 min and ion etching $\tau = 17\ min$ (c)

The XPS spectra (Fig. 21.) point out the occurrence of NiO [74], CeO₂ and Ce₂O₃ oxides [75, 76] on the particles surface. During sputtering a new feature develops at low binding energy side 28($E_B=852.7$ eV), which can be attributed to metallic Ni [77]. The apparition of metallic Ni peak is due to the reach of Ni core after the argon ion bombardment. Furthermore, a small contribution to Ni peak comes also by a loss of oxygen at surface in the sputtering process of NiO [78]. The quantity ratio of cerium oxides CeO₂/Ce₂O₃ and the thickness of NiO layer increase with the annealing temperature. At 800 °C only CeO₂ was detected (Fig. 22.).

3.2.5. Raman measurements

com plem entary method in order to confirm the

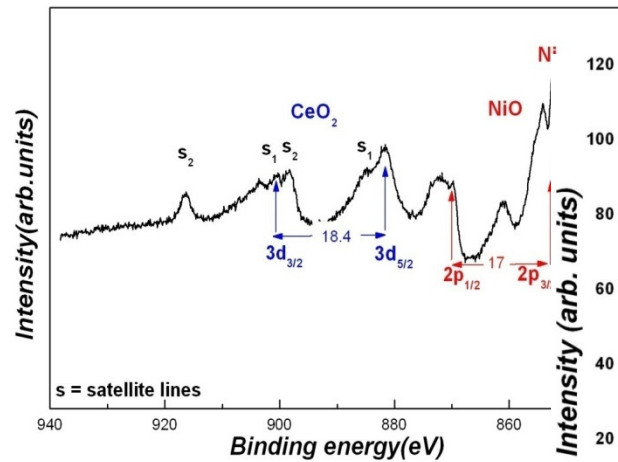
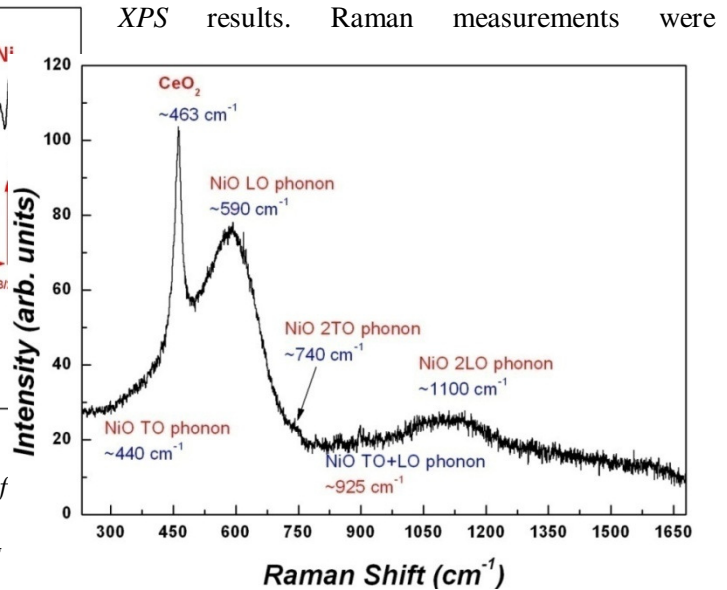


Fig. 22. Ni 2p and Ce 3d core levels spectra of powder oxidized in air at 800 °C for 1h and exposure time to ion etching min.

Raman measurements were used as a

Fig. 21. Ni 2p and Ce 3d core levels line of CeNi₅ powder 600 °C for 1h and exposure time to ion etching $\tau = 10$ min (a), oxidized in air at 600 °C for 1h without sputtering (b) and oxidized in air at 300 °C for 30 min and ion etching $\tau = 17$ min (c)



XPS results. Raman measurements were

performed in Germany, at Technische Universität Chemnitz, based on scattering geometry principle, using a *micro-Raman* installation formed by an *Olympus* microscope coupled with a *Dilon XY 800* triple monochromator. The used laser excitation was 514.5 nm corresponding to Ar^+ , and the resolution was $\sim 2\text{ cm}^{-1}$.

Room temperature Raman spectrum of $CeNi_5$ powder oxidized in air at $800^\circ C$ for one hour is shown in **Fig. 23**. The spectrum is formed by more bands corresponding to NiO and CeO_2 . Raman peak situated at $\approx 463\text{ cm}^{-1}$ corresponds to CeO_2 triple degenerate F_{2g} mode [131]. Several vibration bands corresponding to NiO [132] can also be identified: one-phonon TO (at 440 cm^{-1}) and LO (at 590 cm^{-1}) modes, two-phonons $2TO$ modes (at 740 cm^{-1}), $TO+LO$ (at 925 cm^{-1}) and $2LO$ (at 1500 cm^{-1}) modes.

Fig. 23. Raman spectrum of $CeNi_5$ powder oxidized in air at $800^\circ C$ for one hour

3.2.6. Summary

XRD studies results of $CeNi_5$ powder oxidized in air at different temperatures up to $800^\circ C$, suggest that during the heat treatment Ni metallic clusters covered by NiO , Ce_2O_3 and CeO_2 appear. The average crystallite size of Ni core and the thickness of NiO oxide formed at the surface were evaluated by means of *Cauchy*, *Gauss*, *Voigt* and *GFF* approximations. The obtained results suggest that both Ni and NiO average crystallite size increase with temperature due to recrystallization processes from 34 nm to 77 nm and from 9 nm to 19 nm respectively. *TEM* images confirm the values obtained from *XRLP* approximation results. *XPS* spectra point out the occurrence of NiO , CeO_2 and Ce_2O_3 oxides on the particles surface. Ni metallic component was detected both in valence bands and core levels spectra only after sputtering. For $CeNi_5$ powder oxidized at $800^\circ C$ for an hour only CeO_2 and NiO layers were detected. The Ce_2O_3 / CeO_2 ration depends on heat treatment temperature. *Raman* measurements confirm the formation of NiO and CeO_2 . The small hysteresis loop shift towards negative magnetic fields confirms the presence of ferromagnetic/antiferromagnetic interface.

3.3. Electronic structure and magnetic properties of some compounds belonging to the ternary Al-Dy-Ni metallic system ($AlDyNi$, $AlDyNi_4$, $AlDy_3Ni_8$) [81]

In the ternary metallic system *Al-Dy-Ni*, ten intermetallic compounds with different crystallographic structure were reported [58].

The nearest *Dy* and *Ni* ions neighbourhood, as well as *Ni-Ni*, *Dy-Dy* and *Dy-Ni* distances are different in each compound. This leads to different states of *Ni* ions and also influences the *Dy-Ni* interaction in these compounds.

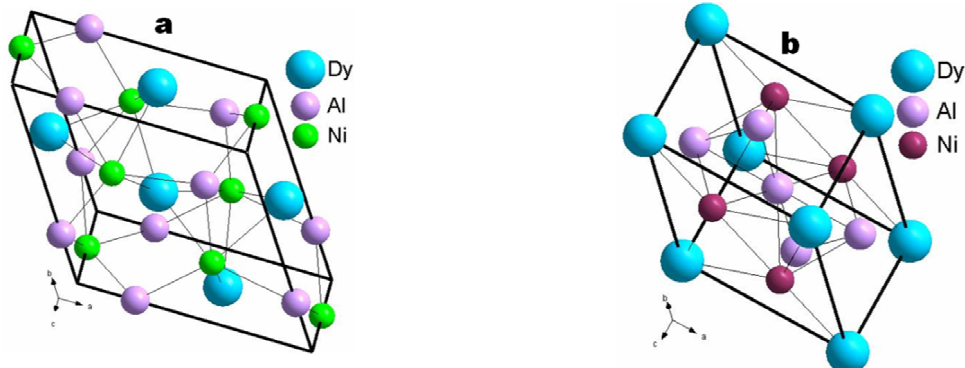
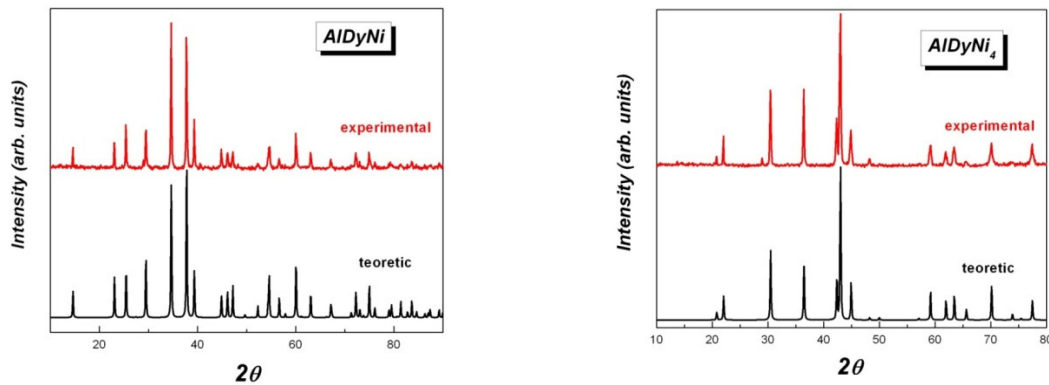
The electronic $3d$ band width of the transition metals (T) is determined by the overlap between the d orbitals of adjacent atoms and depends on the number of nearest neighbours and the hopping integral J_h , which is very sensitive to the T - T distances [82]. On the other hand, the hybridizations between $Ni\ 3d$ and $Dy\ 5d6s$ states with $Al\ 3sp$ states may lead to a partial or complete filling of the $Ni\ 3d$ band. In many rare-earth-nickel compounds, nickel atoms do not carry a magnetic moment because of charge transfer of rare-earth conduction electrons to the $3d$ band [83].

In the next pages the magnetic behaviour and the electronic structure for three of the ten compounds belonging to Al - Dy - Ni system ($AlDyNi$, $AlDyNi_4$ and $AlDy_3Ni_8$) are going to be investigated through X -ray photoelectron spectroscopy (XPS), X -ray diffraction (XRD), static and dynamic magnetic measurements.

3.3.1. Samples preparation and structural characterisation

The same standard arc-melting technique using a water-cold crucible in an argon atmosphere was used in order to prepare the ten samples belonging to Al - Dy - Ni system: $AlDyNi$, $AlDyNi_4$, $AlDy_2Ni_2$, $AlDy_3Ni_8$, $Al_2Dy_3Ni_6$, Al_2DyNi , Al_4DyNi , Al_3DyNi_2 , $Al_7Dy_2Ni_3$ and $Al_{16}DyNi_3$. The purity of the starting materials was 99.9 % for Dy , 99.99% for Ni and 99.999 % for Al .

X -ray powder diffraction measurement showed that only three of the ten compounds are single phases with the expected crystallographic structure type: $AlDyNi$, $AlDyNi_4$ and $AlDy_3Ni_8$ (Fig. 24.)



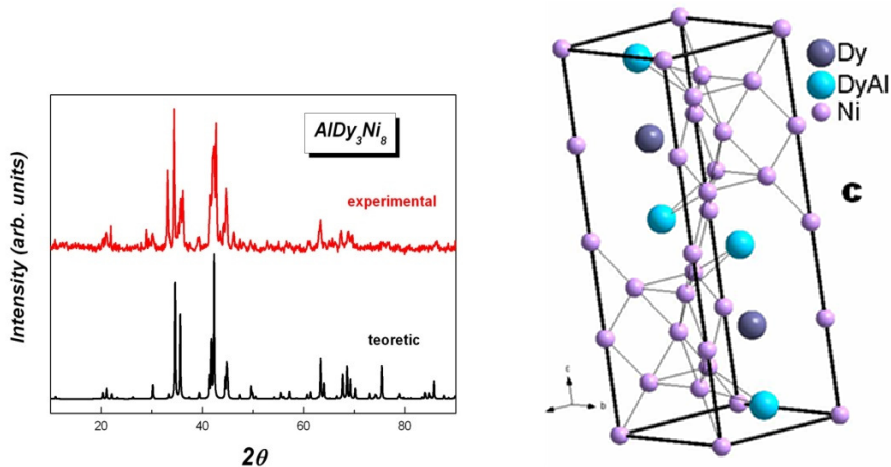


Fig. 24. XRD patterns and unit cells of $AlDyNi$ (a), $AlDyNi_4$ (b) and $AlDy_3Ni_8$ (c) compounds

The lattice parameters corresponding to investigate samples, obtained after refinement are listed in **Tabelul 4**.

Tabelul 4. Structure type and lattice parameters corresponding to $AlDyNi$, $AlDyNi_4$ and $AlDy_3Ni_8$ compounds

Compound	Structure Type	Pearson Symbol	a (nm)	c (nm)
$AlDyNi$	Fe_2P	$hP9$	6.9939	3.8496
$AlDyNi_4$	$CaCu_5$	$hP6$	4.9260	4.0330
$AlDy_3Ni_8$	$CeNi_3$	$hP24$	5.0370	16.1000

3.3.2. Magnetic measurements

In order to elucidate the magnetic behaviour of investigated compounds, several types of magnetic measurements were necessary. The magnetization measurements (**Fig. 25.**) were performed in France, at *Louis Néel Laboratoires from Grenoble*, with a vibrating sample magnetometer (VSM) at 4 K and magnetic fields up to 10 T. The magnetic susceptibility measurements were performed at Cluj, with two different installations: the horizontal Weiss balance belonging to “Ioan Ursu Institute” was used starting from room temperature until 600K and for 5 - 300K temperature range a VSM device from the same institute was employed. The AC susceptibility was also measured using a superconducting quantum interference device (SQUID magnetometer) in the 4.2 - 300K temperature range. These measurements have also been performed in France at *Laboratoire de Crystallographie CNRS, Grenoble*.

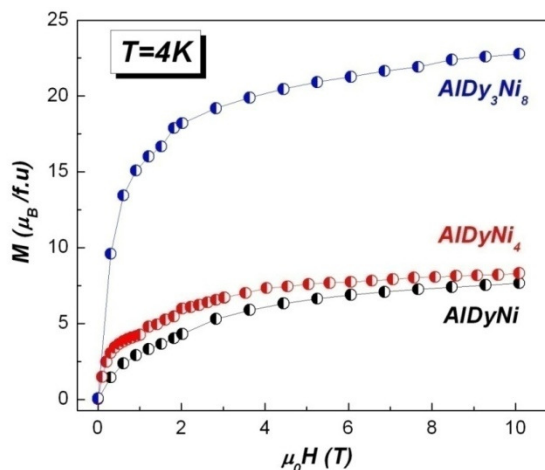


Fig. 25. Magnetization versus external magnetic field at $T=4K$ for $AlDyNi$, $AlDyNi_4$ and $AlDy_3Ni_8$ compounds

The magnetization versus magnetic field dependence is characteristic for ferromagnetic materials. The spontaneous magnetization (**Table 5**) was obtained by extrapolation to $H \rightarrow 0$ of the linear part (in the high fields range) of the $M(H)$ curve. The corresponding values of the magnetic moments per Dy atom in the ordered state are smaller than for free Dy^{3+} ion ($10\mu_B$). This is characteristic for many Dy compounds [84] and may be explained taking into account the of crystal field effect (the ground state of Dy^{3+} ion is ${}^6H_{15/2}$ [42]).

Table 5. Ferromagnetic (T_C) and paramagnetic (θ) Curie temperatures, magnetic moments per formula unit in the ordered (μ) and paramagnetic (μ_{eff}) states

Compound	T_C (K)	μ (μ_B /f.u.)	θ (K)	μ_{eff} (μ_B /f.u.)
$AlDyNi$	25	6	30	10.88
$AlDyNi_4$	14	6.9	6	10.94
$AlDy_3Ni_8$	22	19.2	11	18.33

The real part of the AC susceptibility (χ') is constant in the 75-300K temperature range. Therefore, in order to obtain a better resolution necessary for Curie temperature (T_C) determination, in **Fig. 26**. was plotted only the temperature interval 4-75K. The values of corresponding Curie temperature are also given in **Table 5**. In case of $AlDyNi_4$ compound $T_C = 14K$. This value is in good agreement with earlier measurements of Tolinski *et al.* [85]. In the high temperature range the magnetic susceptibility obeys a Curie-Weiss law $\chi=C/(T-\theta)$ (**Fig. 27**.). The effective magnetic moment per Dy atom in $AlDyNi$ compound, determined from the Curie constant, is $10.88 \mu_B$, bigger than the value for Dy^{3+} free ion ($10.6\mu_B$). This value can be explained if we consider that Dy 5d electrons are polarized by 4f-5d local exchange interactions. Because this polarization is in the same direction as that of the localized 4f moments, an excess magnetic moment per Dy atom would be expected. This is in agreement with many experimental findings that the 5d electrons contribute to the total moment per rare-earth atom [86]. In addition to this contribution, in $AlDyNi_4$ and $AlDy_3Ni_8$ compounds, the Ni atoms also carry a small magnetic moment confirmed by XPS spectra. The small Ni contribution appears due to some spin fluctuations at the Ni atoms position.

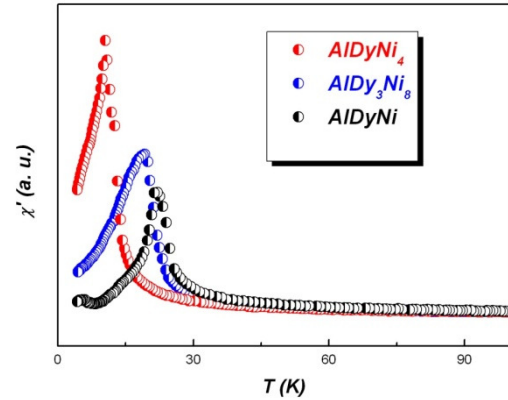


Fig. 26. The χ' dependence as a function of temperature of $AlDyNi$, $AlDyNi_4$ and $AlDy_3Ni_8$ compounds

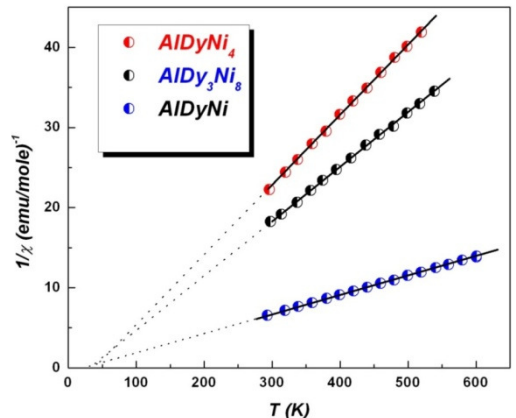


Fig. 27. The reciprocal susceptibility versus temperature for $AlDyNi$, $AlDyNi_4$ and $AlDy_3Ni_8$ compounds

In case of $AlDyNi_4$ and $AlDy_3Ni_8$ magnetic susceptibility measurements below room temperature were performed (**Fig. 28**). The corresponding paramagnetic *Curie* temperatures are $6K$ for $AlDyNi_4$ and $11K$ for $AlDy_3Ni_8$ respectively.

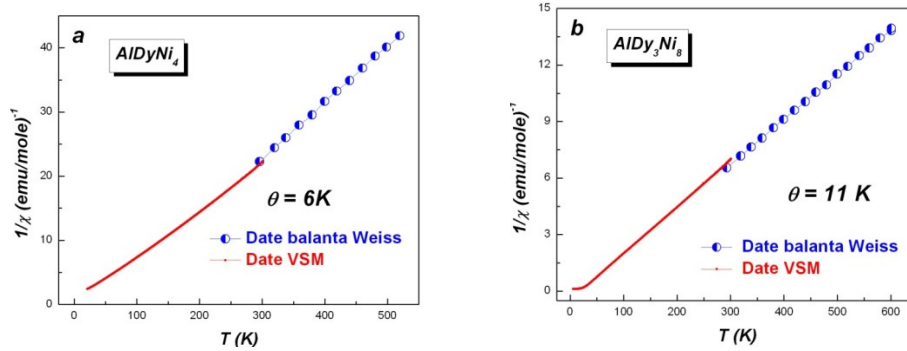


Fig.28. Thermal variation of reciprocal susceptibility measured with Weiss balance (blue lines and circles) and VSM (red lines and circles) in case of $AlDyNi_4$ (a) and $AlDy_3Ni_8$ (b)

The $AlDyNi_4$ and $AlDy_3Ni_8$ compounds order ferrimagnetically below the corresponding *Curie* temperatures. This thing is proved by the values of paramagnetic *Curie* temperature which are smaller compared to *Curie* temperature associated to the ordered magnetic state ($\theta < T_c$) (**Table 5**). Since the magnetic moment per Ni atom is smaller compared to Dy magnetic moment, we can consider that we have to deal with ferromagnetic materials. In the high temperature range the magnetic susceptibility obeys a *Curie-Weiss* law. The strong hybridization between Ni 3d, Dy 5sp and Al 3sp leads to a gradual filling of Ni 3d band. In case of $AlDyNi_4$ and $AlDy_3Ni_8$, the Ni atoms carry a small magnetic moment. For $AlDyNi$ the Ni 3d band is completely filled, so Ni atoms bring no contribution. The total filling of Ni 3d band in case of $AlDyNi$, is due to the high number of Al and Dy atoms in the Ni atoms first vicinity.

3.3.3. XPS spectra

The electronic structure of $AlDyNi$, $AlDyNi_4$ and $AlDy_3Ni_8$ is revealed by XPS valence band and core level spectra analyse. All the spectra were recorded at room temperature, using a monochromatized Al K- α source. The pressure in the ultra-high vacuum chamber was in the 10^{-10} mbar range during the measurements. The samples were cleaved in situ. The contamination of the fresh cleaned surface inside the preparation chamber was checked by monitoring the C 1s levels. It is well known that rare earths elements present a high oxygen affinity. A slight sample contamination can be observed at 284.5 eV.

Valence band spectra

Fig. 29. shows the valence band spectra of analysed compounds compared to pure metallic Ni and reference compound AlNi. The main contribution to the valence band spectra is given by the Ni 3d and Dy 4f electrons. The Ni 3d band is situated close to the *Fermi* level while Dy 4f band is

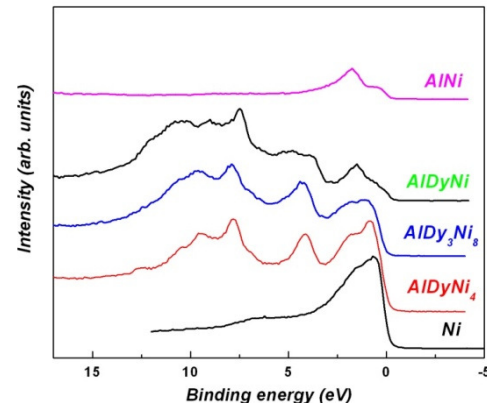


Fig. 29. Valence band spectra of $AlDyNi$, $AlDyNi_4$, $AlDy_3Ni_8$ and of reference Ni metal and AlNi

more localized and splitted in several components. The reference compound is a Pauli paramagnet with the *Ni 3d* band completely filled [87].

Ni 3d band centroids are shifted towards higher binding energy relative to metallic *Ni*, suggesting a partial filling of the *Ni 3d* band due to a strong hybridization between *Ni 3d*, *Dy 5sp* and *Al 3sp* states. The position of valence band maximum at ~ 1.5 eV in case of *AlDyNi* is in good agreement with that observed in case of Pauli paramagnet *AlNi*, and confirms the complete filling of *Ni 3d* band.

Core-level XPS spectra

Ni 2p core level XPS spectra

Ni 2p core-level lines of investigated compounds together with pure metallic *Ni* spectra are shown in **Fig. 30**.

The decrease in the satellite structure intensity of *Ni 2p* line compared to pure *Ni* confirms the partial filling of the *Ni 3d* band. These spectra also indicate that *Ni* atoms carry a magnetic moment in *AlDyNi₄* and *AlDy₃Ni₈* compounds, which in the ordered state is orientated antiparallel to the *Dy* magnetic moment due to the *4f-5d-3d* coupling. For *AlDyNi* the *Ni 2p* satellite structure disappears, suggesting that *Ni 3d* band is completely filled and *Ni* atoms have no contribution to the total magnetic moment.

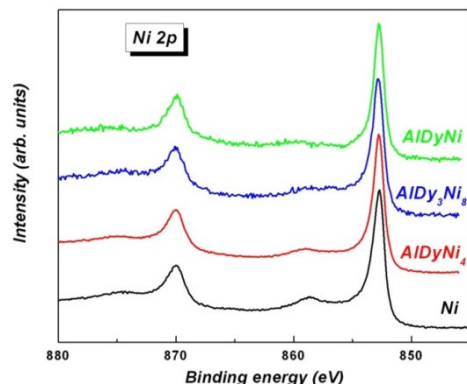


Fig. 30. *Ni 2p* core-level lines of investigated *AlDyNi*, *AlDyNi₄*, *AlDy₃Ni₈* compounds compared to *Ni* metal

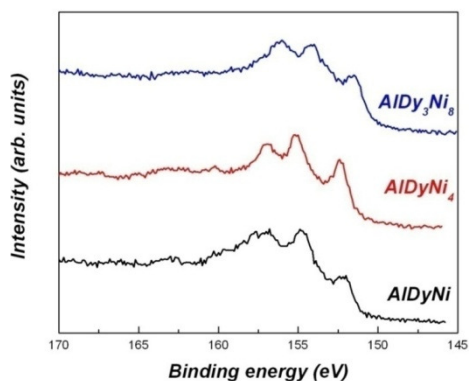


Fig. 31. *Dy 4d* core-level lines of *AlDyNi*, *AlDyNi₄* and *AlDy₃Ni₈*

Spectrele XPS ale nivelelor interne Dy 4f

In **Fig. 31**, are shown the *Dy 4d* lines for all investigated compounds. A chemical shift smaller than 0.4 eV, comparing to pure *Dy* [72], was evidenced. Furthermore the exchange splitting of *Dy 4d* core level in all three compounds is similar to that found in pure *Dy*, suggesting that *Dy 4f* levels are not affected by alloying.

3.3.4. Summary

The electronic and magnetic properties of *AlDyNi*, *AlDyNi₄* and *AlDy₃Ni₈* were studied using X-ray photoelectron spectroscopy (XPS), X-ray diffraction (XRD), static and dynamic magnetic measurements. The three compounds are single phases and crystallize in the *Fe₂P*, *CaCu₅* and *CeNi₃* structure types, respectively. All the investigated samples order ferromagnetically below the corresponding Curie temperatures. At high temperature the magnetic susceptibility obey the Curie-Weiss law. XPS valence band and *Ni 2p* spectra indicated the presence of small magnetic moment on *Ni* sites in *AlDy₃Ni₈* and *AlDyNi₄*, and a complete filling of *Ni 3d* band in *AlDyNi*. The complete filling of *Ni 3d* band in *AlDyNi* compound is due to the high number of *Al* and *Dy* atoms in the *Ni* atoms vicinity. The polarization of *5d* electrons by the local exchange interaction *4f-5d* gives rise to an excess magnetic moment of *Dy* ions in the paramagnetic state of investigated compounds.

3.4. *Electronic structure and magnetic properties of $MnSb_{1-x}Bi_x$ ($x=0, 0.2, 0.5$ and 0.95) system* [88]

The intermetallic compound $MnBi$ received considerable attention since its favorable magneto-optical properties were recognized [89]. The high uniaxial magnetic anisotropy [90] at room temperature and the magneto-optical properties have attracted the interest of scientific community because of its possible applications in permanent magnets [91] and erasable magneto-optical memory devices [92]. The binary compound $MnBi$ crystallizes into two phases: the lower-temperature hexagonal ferromagnetic phase (*LTP*) and the high temperature orthorhombic paramagnetic phase (*HTP*) with a structural phase transition at 628 K [93]. Numerous attempts have been made for the purpose of obtaining single-phase $MnBi$, such as arc melting and rapid solidification methods [94, 95], but formation of Mn precipitations and Bi matrix could not be avoided [96]. At present, no single-phase $MnBi$ has been prepared. In order to oversee this impediment many efforts have been made to stabilize $MnBi$ by varying its stoichiometry or by alloying it with a third element like Cu , Al , Nb , Si , etc., without any success [97-99]. The electronic structure of $MnBi$ indicates that Mn atom possesses a magnetic moment of $3.6 \mu_B$, and that the Bi atom has a magnetic moment of $-0.15 \mu_B$ which is due to the $s-d$ and $p-d$ hybridization between Bi and Mn atoms [93]. On the other hand, the ferromagnetic compound $MnSb$ has an electronic structure similar to $MnBi$ and also crystallizes in two different structures: nickel-arsenide (*NiAs*) and zinc-blende (*ZB*). $MnSb$ presents a $3d^{5.5}$ configuration of Mn atom, with a magnetic moment of $3.5 \mu_B$ on the Mn sites, and $-0.06 \mu_B$ on the Sb sites and a Curie temperature well above room temperature ($T_c=587$ K) [32, 33, 100]. Since both $MnBi$ and $MnSb$ have a hexagonal structure of *NiAs* type, it is possible for new ternary $Mn-Bi-Sb$ system with an appropriate constitution to form a hexagonal structure too.

The purpose of this study was to obtain a new material with improved qualities by studying the structural and electronic changes induced by the substitution of Sb with Bi in $MnSb_{1-x}Bi_x$ ($x=0, 0.2, 0.5$, and $x=0.95$) system.

3.4.1. *Preparation and structural characterisation*

At the beginning the main idea was to obtain single phase $MnBi$ compound, through classical argon arc melting method. For this purpose we have made several attempts, unfortunately without any success. After these failures, the study direction was changed and the main goal became the stabilisation of $MnBi$ phase through alloying with nonmagnetic elements. The same argon arc melting method was used in order to prepare several compounds obtained by the substitution of Bi with Sn and Al in $MnBi$ compound, but the obtained results were not satisfactory.

Taking into account that in normal conditions it was not possible to obtain single phase $MnBi$, and that $MnBi$ is isostructural with $MnSb$ compound, which can be easily obtained at room temperature through argon arc melting method, the purpose of this study was to obtain a new material with improved qualities by studying the structural and electronic changes induced by the substitution of Sb with Bi in $MnSb$, resulting in the $MnSb_{1-x}Bi_x$ system. Four samples belonging to $MnSb_{1-x}Bi_x$ system were prepared by argon arc melting method for the following Bi concentration: $x=0, 0.2, 0.5$, and $x=0.95$. The purity of the starting materials was 99.99% for Mn and Sb and 99.9% in case of Bi .

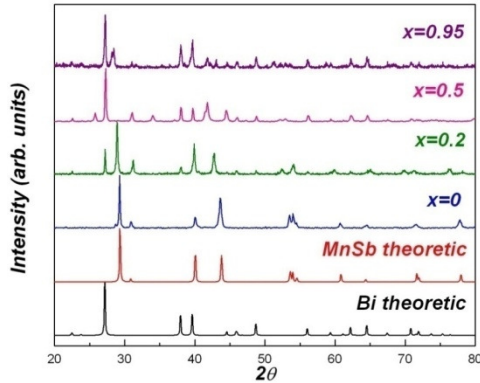


Fig. 32. X-ray diffraction patterns of $MnSb_{1-x}Bi_x$ ($x=0, 0.2, 0.5$ and 0.95) alloys and theoretical pure Bi and $MnSb$ spectra

The homogeneity of the as-prepared samples was checked by conventional X-ray powder diffraction. The preparation quality of the samples was verified by XRD. The XRD patterns for the investigated samples are given in **Fig. 32**, together with theoretical pure Bi and $MnSb$ patterns.

The samples obtained by the substitution of Sb with Bi in $MnSb$ have the same hexagonal crystallographic $NiAs$ structure type ($MnSb_{1-x}Bi_x$ solid solution) corresponding to the parent compound and also observed in case of $MnBi$. One can see the presence of some pure Bi peaks in all patterns. The presence of these peaks is due to Bi segregation during the preparation process. The pure Bi phase is small compared to $MnSb_{1-x}Bi_x$ phase, except for $x=0.95$ where it succeeds the

nickel-arsenide structure type phase.

3.4.2. Magnetic measurements

In 1904, *Heusler* reported the ferromagnetic nature of $Mn-Bi$ alloys [101]. *Tielman* has been the first who published the associated theoretical magnetization curve of $MnBi$ compound [102]. Theoretical calculations have shown that monodomain $MnBi$ particles show a high coercitive field $H_c \sim 1.2 T$ [103], due to the hexagonal symmetry, which also denotes a high anisotropy.

Fig. 33. shows the hysteresis loop obtained by *Saha et al.* [104] for the low temperature phase (LTP) of $MnBi$. The magnetisation curve was measured at room temperature. The obtained value for coercitive field is $0.66 kOe$.

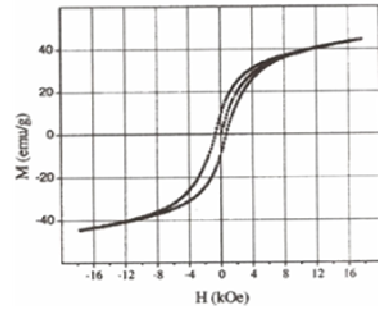


Fig. 33. Magnetisation versus external field dependence in case of $MnBi$ - low temperature phase (LTP)

The same magnetisation measurements using a VSM were performed in case of investigated compounds. The hysteresis loops corresponding to $MnSb_{0.8}Bi_{0.2}$ and $MnSb_{0.5}Bi_{0.5}$ are given in **Fig. 34**. The curves were recorded at $5K$, in fields up to $3 T$. The inset of each figure shows the magnetic behaviour in the very small field region.

In case of $MnSb_{0.8}Bi_{0.2}$, the value of saturation magnetisation (M_s) can be obtained from hysteresis curve by extrapolating the magnetisation at zero magnetic fields (**Fig. 34a**). The obtained value was used in the calculation of magnetic moment per formula unit ($f.u.$). The magnetic moment associated to $MnSb_{0.8}Bi_{0.2}$ is equal to $2.85 \mu_B/f.u.$. This value is smaller than that measured in case of $MnSb$ parent compound ($3.3-3.5 \mu_B/f.u.$), due to the formation of $MnSb_{1-x}Bi_x$ solid solution and to the presence of some unreacted Bi . The anisotropy field for $MnSb$ is $H_a=0.26T$. The substitution of Sb with Bi in $MnSb$ leads to the formation of improved materials with higher magnetic anisotropy. As an example, in case of $MnSb_{0.8}Bi_{0.2}$ the value of anisotropy field is $\approx 1.5T$, almost six times bigger than that of starting compound.

For uniaxial and polycrystalline *MnSb* thin films, the reported coercitive fields have values $(110-200)Oe$ [105]. From the insets of **Fig. 34** which present the magnetization in the small field region a considerable increasement of coercitive fields value can be observed in case of $MnSb_{0.8}Bi_{0.2}$ ($H_c = 235 Oe$) and $MnSb_{0.5}Bi_{0.5}$ ($H_c = 420 Oe$).

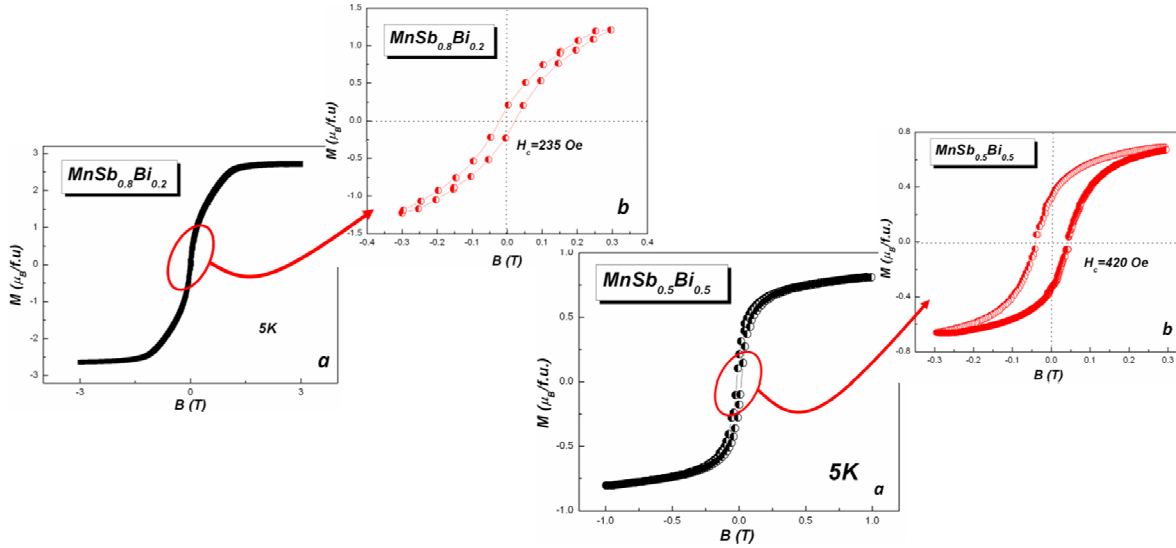


Fig. 34. Hysteresis loop for $MnSb_{0.8}Bi_{0.2}$ and $MnSb_{0.5}Bi_{0.5}$

3.4.3. XPS spectra

XPS core level and valence band spectra can provide important information regarding the electronic structure. Just like in case of previous analysed samples, the surface contamination was checked by monitoring the oxygen and carbon *1s* core levels. Contamination is almost absent, thus the XPS spectra are representative of the bulk.

Valence band spectra

For *Al K- α* radiation the photoionization cross section of *Mn*, *Sb* and *Bi* are comparable; therefore the valence band spectra of $MnSb_{1-x}Bi_x$ alloys are dominated by three main contributions: one given by *Sb 5p*, another one from *Mn 3d* and finally the *Bi 6p* states. **Fig. 35** shows the valence band spectra of $MnSb_{1-x}Bi_x$ ($x = 0, 0.2, 0.5$ and 0.95) alloys. One can observe that the substitution of *Sb* with *Bi* in *MnSb* leads to the appearance of a new feature at higher binding energy, which is characteristic for the *MnBi* phase. The intensity of this feature increases with the increasement of *Bi* concentration.

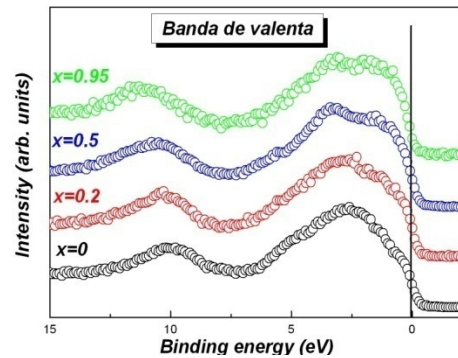


Fig. 35. XPS valence band spectra of $MnSb_{1-x}Bi_x$ ($x = 0, 0.2, 0.5$ and 0.95) alloys

The spectral feature situated at about $10\text{--}11\text{ eV}$ is assigned to $Sb\ 5s$ and $Bi\ 6s$ states [47]. The displacement of this feature is generated by the contribution brought by $Bi\ 6s$ levels (10.5 eV).

A better understanding of the main characteristics in the valence band requires a comparison with

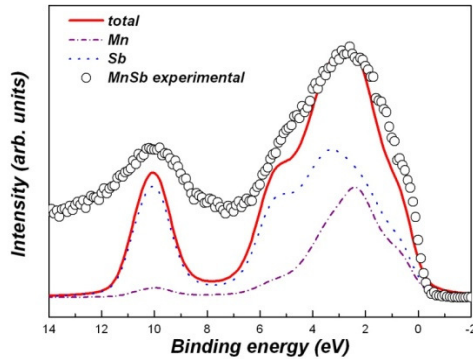


Fig. 36. Calculated (lines) and experimental (circles) XPS valence

the XPS valence band spectra of $MnSb$ calculated with the *Munich SPR-KKR* package (**Fig. 36**).

The computed XPS valence band spectrum of $MnSb$ is in good agreement with the experimental results, indicating that the measured spectrum is representative of the bulk. Taking into account the similarities of the $MnSb$ and $MnBi$ electronic structures, one may suppose that the calculated XPS valence band spectrum of $MnSb$ is also representative for the $MnSb_{1-x}Bi_x$ solid solutions.

Core levels XPS spectra

Mn 2p core level XPS spectra

$Mn\ 2p$ XPS spectra of $MnSb_{1-x}Bi_x$ ($x = 0, 0.2, 0.5$ and 0.95) system (**Fig. 3.7**) present a spin-orbit splitting of $\sim 11\text{ eV}$, which can be identified in the distance between the centres of energy of the $2p_{3/2}$ and $2p_{1/2}$ states. The substitution of Sb by Bi in $MnSb$ brings no significant changes in the $Mn\ 2p$ band.

In case of atomic Mn , experimental and theoretical results revealed a fine structure of the $2p$ photoelectron spectrum caused by the Coulomb interactions of the $2p$ hole and $3d$ valence electrons [106]. **Fig. 38.** shows the fitting results of $Mn\ 2p_{3/2}$ XPS spectra for the investigated alloys. These fitting were performed using *Unifitt* program considering four components and a satellite line.

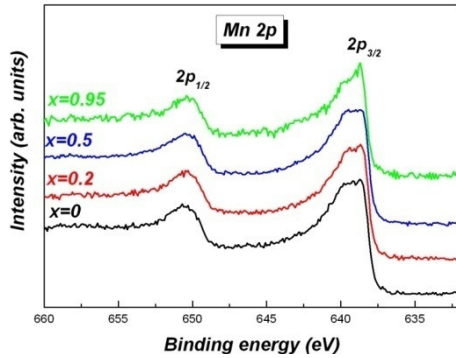
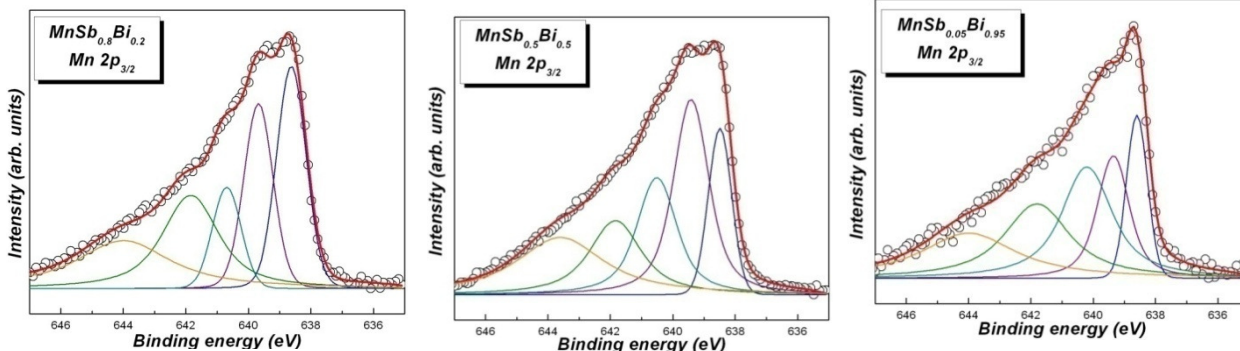


Fig. 37. XPS $Mn\ 2p$ core level spectra of $MnSb_{1-x}Bi_x$ ($x = 0, 0.2, 0.5$ and 0.95) alloys



0.5 and 0.95) alloys superposed on the measured spectra (circles)

Fig. 38. Curve fitting results (solid lines) of $Mn\ 2p_{3/2}$ core level spectra of $MnSb_{1-x}Bi_x$ ($x = 0, 0.2,$

Just like in case of previous analysed $In_{1-x}Mn_xSb$ system, the results were obtained considering four components and a satellite line. The full width at half maximum ($HWHM$) of each multiplet peak was considered between 1 eV and 1.5 eV , with a 0.4 eV Lorentian contribution (accounting the $Mn\ 2p$ hole states lifetime [46]) and a $0.6\text{--}0.8\text{ eV}$ Gaussian contribution (accounting for the instrumental broadening).

The relative intensities of these states vary depending on the *Mn* atomic environment, reflecting the changes induced to the properties of *Mn 3d* states.

The corresponding binding energies of fitted multiplet splitting components and the mean energy separation between the four components, which corresponds to the exchange splitting of the *Mn 2p* core-hole states, are listed in the table below (**Table 6**).

In the investigated samples the mean energy separation between the four components has a value between *1.01 eV* and *1.12 eV*. These values confirm the formation of *MnSb_{1-x}Bi_x* solid solution by the substitution of *Sb* with *Bi* in *MnSb* compound. Since the exchange splitting Δ_{ex} is approximately the same in all alloys one may suppose that the *Mn 3d* states in *MnSb_{1-x}Bi_x* system are not affected by alloying.

Table 6. Fitting parameters for *Mn 2p_{3/2}* XPS spectra of *MnSb_{1-x}Bi_x* ($x= 0, 0.2, 0.5$ and 0.95) alloys. Δ_{ex} denotes the mean exchange splitting between the sublevels

x	Binding energy (eV)				Δ_{ex} (eV)
	Component 1	Component 2	Component 3	Component 4	
0	638.5	639.3	640.3	641.5	1.01
0.2	638.6	639.6	640.7	641.8	1.07
0.5	638.4	639.4	640.5	641.8	1.12
0.95	638.6	639.3	640.1	641.7	1.06

Sb 3d core level XPS spectra

The *Sb 3d* XPS core level spectra of *MnSb_{1-x}Bi_x* ($x= 0, 0.2,$ and 0.5) system are shown in **Fig. 39**.

The lack of *O 1s* peak at *531eV* binding energy in the *Sb 3d* core level spectra indicates that contamination is absent and proves the good quality of the investigated sample. The small chemical shifts observed in the *Sb 3d* core level spectra of *MnSb_{1-x}Bi_x* may be explained by the changed induced in the *Sb* atoms vicinity.

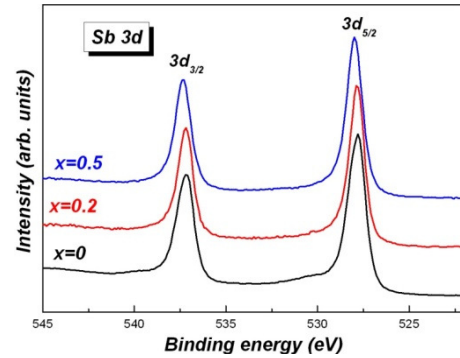


Fig. 39. XPS *Sb 3d* core level spectra of *MnSb_{1-x}Bi_x* ($x= 0, 0.2$ and 0.5) alloys

3.4.4. Summary

Until now no single-phase *MnBi* has been prepared. In order to oversee this impediment we have tried to stabilize *MnBi* phase by alloying it with *Sb*. The substitution of *Sb* by *Bi* in *MnSb* leads to the formation of new and improved compounds which preserve the same crystallographic structure as the parent compound. The X-ray diffraction measurements indicate the formation of *MnSb_{1-x}Bi_x* solid solution. For higher *Bi* concentration ($x=0.95$) one can observe that a mixture of pure metallic *Bi* and *MnSb_{1-x}Bi_x* phase appears. The presence of unreacted *Bi* is due to the segregation during the preparation process. Magnetic measurements at low temperatures confirm the formation of improved materials with higher magnetic anisotropy and higher coercive field. XPS valence band, *Mn 2p* and *Sb 3d* core level spectra have confirmed the formation of *MnSb_{1-x}Bi_x* solid solution. The computed XPS valence band spectrum of *MnSb* is in good agreement with the experimental results, indicating that the measured spectrum is representative of the bulk. The *Mn 2p_{3/2}* core levels exhibit a multiplet structure arising from the exchange interactions between the core hole and the open *3d* shell. The *Mn 3d* states in *MnSb_{1-x}Bi_x* do not change appreciable by alloying.

REFERENCES

- [1] P.O.M. Dirac, *Proc. Roy. Soc. Lond. A* **123**, 714-733 (1929)
- [2] J. H. Van Vleck, *The Theory of Electric and Magnetic Susceptibilities*, Oxford University Press, Oxford (1932)
- [3] M. A. Ruderman and C. Kittel, *Phys. Rev.* **96**, 99 (1954)
- [4] T. Kasuya, *Prog. Theor. Phys.* **16**, 58 (1956)
- [5] K. Yoshida, *Phys. Rev.* **106**, 893 (1957)
- [6] P. Weiss, *J. Phys. Radium* **6**, 661 (1907)
- [7] A. H. Morrish, *The physical principles of magnetism*, New York: John Wiley and Sons. (1965)
- [8] E. C. Stoner, *Proc. Roy. Soc. London* **A165**, 372 (1938)
- [9] E.C. Stoner, *Proc. Roy. Soc.* **A169**, 339 (1939)
- [10] J.H. Van Vleck, *Rev. Mod. Phys.* **25**, 220 (1953)
- [11] P.W. Anderson, *Phys. Rev.* **124**, 41 (1961)
- [12] J. Friedel, *Can. J. Phys.* **34**, 1190 (1956); *Nuovo Cimento Suppl.* **7**, 287 (1958)
- [13] S. Alexander and P.W. Anderson, *Phys. Rev.* **133**, A1594 (1964)
- [14] T. Moriya, *Prog. Theor. Phys.* **33**, 157(1965)
- [15] K. Sigbahn, C. Nordling, A.Fahlman, R. Nordberg, K. Hamrin, J. Hedman, G. Johansson, T. Bergmark, S.E. Karlsson, I. Lindgren, ESCA-Atomic, *Molecular and Solid State Structure Studied by Means of Electron Spectroscopy*, Almquist and Wicksell, Uppsala (1967)
- [16] K. Sigbahn, C. Nordling, G. Johansson, J. Hedman, P.F. Heden, K. Harmin, U. Gelius, T. Bergmark, L.O. Werme, R. Manne, Y. Baer, *ESCA Applied to free molecules*, North Holland Amsterdam (1969)
- [17] W.E. Spicer, *Phys. Rev.* **112**, 114 (1958)
- [18] N. Berglund and W. E. Spicer, *Phys. Rev.* **136**, A1044 (1964)
- [19] S. Hüfner, *Photoelectron Spectroscopy Principles and Applications*, Springer-Verlag, Berlin (1995)
- [20] V. K. Pecharski and Z. V. Zavalij, *Fundamentals of Powder Diffraction and Structural Characterization of Materials*, Kluwer Academic Publisher, Boston (2003)
- [21] G. Nolze and W. Kraus, *PowderCell 2.3 Program*, BAM Berlin (2000)
- [22] H. Ebert, *Electronic Structure and Physical Properties of Solids*, vol. 535, pp. 191; editor: H. Dreysse, Lecture Notes in Physics, Springer, Berlin, (2000); *The Munich SPRKKR package, Version 3.6*, <http://olymp.cup.uni-muenchen.de/ak/ebert/sprkkkr>
- [23] P. Weinberger, *Electron Scattering Theory for Order and Disordered Matter*, University Press, Oxford (1990)
- [24] A.Gonis, *Green Function for Ordered and Disordered Systems*, North-Holland, Amsterdam (1992)
- [25] P. Strange, *Relativistic Quantum Mechanics*, University Press, Cambridge (1998)
- [26] L. Rednic, I. Deac, E. Dorolti, M. Coldea, V.Pop, V. Rednic, M. Neumann, *Cent. Eur. J. Phys.*, DOI: 10.2478/s11534-009-0140-7
- [27] L. Rednic, I. Deac, E. Dorolti, M. Coldea, V.Pop, V. Rednic, M. Neumann, *J. Optoelectron. Adv. Mat. – Symposia* **2** (1), 27-30 (2010)
- [28] G. A. Prinz, *Science* **282**, 1660 (1998)
- [29] G. Avery, D. W. Goodwin, W. D. Lawson and T. S. Moss, *Proc. Phys. Soc.* **B 67** 761-767 (1954)
- [30] T. Wojtowicz, W. L. Lim, X. Liu et al., *Physica E* **20** (3-4), 325 (2004)
- [31] V.M. Novotortsev, I.S. Zakharov, A.V. Kochura, S.F. Marenkin, R. Laiho, E. Lehderanta, A. Lashkul, A. G. Veresov, A.V. Molchanov and G.S. Yurev, *Russian Journal of Inorganic Chemistry*, 51, 1627 (2006)

- [32] J.W. Allen and W. Stutius, *Solid State Commun.* **20**, 561(1976)
- [33] W.J. Takei, De.E. Cox and G. Shirane, *Phys Rev.* **129(5)**, 2008 (1963)
- [34] P. Kushwaha, R. Rawat and P. Chaddah, *J. Phys. Condens Matter* **20** (2008)
- [35] C. Estournes, T. Lutz, J. L. Guille, *J. Non-Cryst. Solids* 197, 192(1996)
- [36] V.S. Goncharov and M.V. Ryzhkovskii, *Pis'ma Zh. Tekh. Fiz.* **27 (13)**, 39 (2001)
- [37] Zheng Rongkun, *Exchange bias in magnetic nanoparticles*, Thesis, Hong-Kong, University of Science and Technology (2004)
- [38] F. J. Darnell, E.H. Cloud and H.S. Jarrett, *Physical Review* **130(2)**, 647(1963)
- [39] R. Harris M. Plischke and M.J. Zuckermann, *Phys. Rev. Lett.* **31**, 160 (1973)
- [40] Chao-Cheng Lin, Chih-Huang Lai, D.H. Wei, Y. J. Hsu, Han-Ping D. Shieh, *J. Appl. Phys.* **95**, 6846 (2004)
- [41] T. Hori, H. Shiraishi and Y. Nakagawa *J. Appl. Phys.* **79** (8), 6633(1996)
- [42] Ch. Kittel, *Introduction to Solid State Physics*, Wiley, New York (1975)
- [43] H. Ebert, *J.Phys: Condens. Matter* **1**, 9111(1989)
- [44] S. Plogmann et al., *Phys. Rev B* **60**, 6428 (1999)
- [45] V. Rednic, M. Coldea, S.K. Mendiratta, M. Valente, V. Pop, M. Neumann, L. Rednic, *J. Magn. Magn. Mat.* (2009), doi:10.1016/j.jmmm.2009.06.020
- [46] M.O. Krause and J. H. Oliver, *J. Phys. Chem. Ref. Data* 8, 329(1979)
- [47] L. Rednic, M. Coldea, I. G. Deac, V. Rednic, N. Aldea, M. Neumann – accepted for publication in *Modern Phys. Lett. B*
- [48] L. Rednic, M. Coldea, V. Rednic, N. Aldea – accepted for publication in *Studia Physica*
- [49] S. Gangopadhyay, G. C. Hadjipanagis, C. M. Sorobsen, K. J. Klabunde, *MRS Symp. Proc.* **206**, 55 (1991)
- [50] W. Gong, H Li, Z. Zhao, J. Chen, *J. Appl. Phys.* **69**, 5119 (1991)
- [51] T. Hayashi, T. Ohno, S. Yatsuya, R. Uyeda, *Japanese J. Appl. Phys.* **16** , 705 (1977)
- [52] M. B. Stern, Y. Cheng, *J. Appl. Phys.* **75**, 6894 (1994)
- [53] A. Gavrin, C. L. Chien, *J. Appl. Phys.* **73**, 6949 (1933)
- [54] J. M. Broto, J. C. Ousset, H. Rakoto, S. Askenazy, Ch. Dufor, M. Brien, P. Mauret, *Solid State Commun.* **85**, 263 (1993)
- [55] J. P. Wang, D. H. Han, H. L. Luo, N. F. Gao, Y. Y. Liu, *J. Magn. Mater.* **L251**, 135 (1994)
- [56] A. H. Morrish, *The Physical Principles of Magnetism*, John Wiley and Sons, 1965
- [57] K. B. Sundaram, P. F. Wahid, O. Melendez, *J. Vac. Sci. Technol.* **A15**, 52 (1997)
- [58] P. Villar and D. L. Calvert, *Pearson's Handbook of Crystallographic Data for Intermetallic Phases vol. 1* Cleveland, OH: American Society of Metals (1994)
- [59] M. Coldea, D. Andreica, M. Bitu, V. Crisan, *J. Magn. Mater.* **157/158**, 627 (1996)
- [60] L. Nordström, M.S.S. Brooks, and B. Johansson, *Phys.Rev.* **B 46**, 3458 (1992)
- [61] H. P. Klug and L. E. Alexander, *X-Ray Diffraction Procedures – For Polycrystalline and Amorphous Materials*, John Wiley & Sons, Inc. (1974)
- [62] B.E. Warren, *X-Ray Diffraction*, Dover Publications, Inc., New York (1990)
- [63] D. Balzar, *J. Res. Natl. Inst. Stand. Technol.* **98**, 321 (1993)
- [64] N. Aldea, A. Gluhoi, P. Marginean, C. Cosma, Xie Yaning, *Spectrochim. Acta Part B*, **55**, 997 (2000)
- [65] R. A. Young, *The Rietveld method*, International Union of Crystallography, Oxford University Press (1993)
- [66] D. Grignoux, F. Givord, R. Lemaire, H. Launois and F. Sayetat, *J. Physique* **43**, 173 (1982)
- [67] T. Moriya, *J. Magn. Mater.* **14**, 1 (1979)
- [68] J. Nogues and I. K. Schuller, *J. Magn. Magn. Mater.* **192**, 203-232 (1999)

- [69] A. E. Berkowitz, Kentaro Takano, *J. Magn. Magn. Mat.* **200**, 552 (1999)
- [70] J. C. Fuggle, F. U. Hillebrecht, Z. Zolnerek and R. Lässer, *Physical Review B* **27**, 12, 7330 (1983)
- [71] J. K. Lang, Y. Baer and P. A. Cox, *J. Phys.* **F. 11**, 121(1981)
- [72] Y. Baer, H. R. Ott, J. F. Fuggle and L. E. De Long, *Phys. Rev. B.* **24**, 5384 (1981)
- [73] J. C. Fuggle, F. U. Hillebrecht, Z. Zolnerek, Ch. Freiburg and M Campagna, in *Valence Instabilities*, edited by P. Wahter and H. Boppart (Nord-Holand, Amsterdam, 1982), p. 267
- [74] G.K. Wertheim, S. Hüfner, *Phys. Rev. Lett.* **28**, 1028 (1972)
- [75] J. G. Clabes, *J. Vac. Sci. Technol.* **A 5**, 2887 (1988)
- [76] K. B. Sundaram, P. F. Wahid, O. Melendez, *J. Vac. Sci. Technol.*, **A15**, 52 (1996)
- [77] S. Uhlebrock, Chr. Scharfschwerdt, M. Neumann, G. Illing and H-J Freund, *J. Phys.: Condens. Matter* **4**, 7973-7978 (1992)
- [78] A.R. Gonzales-Elipse, G. Munuera and S. Witzel, *Z. Phys.* **B 83**, 185 (1991)
- [79] M. Radović, Z. D. Dohčević-Mitrović, A. Golubović, B. Matović, M. Šćepanović and Z. V. Popović, *Acta Physica Polonica A 116*, 614 (2009)
- [80] R. E. Dietz, W. F. Brinkman, A. E. Meixner, H. J. Guggenheim, *Phys. Rev. Lett.* **27**, 814 (1971)
- [81] V. Rednic, M. Coldea, L. Rednic, L.G. Pascut, N. Aldea, S. Pintea and M. Neumann, *Journal of Physics: Conf Series* **182**, 012077 (2009)
- [82] J. Mathon, *Contemporary Physics* **32**, 143 (1991)
- [83] H. R. Kirchmager, E. Burzo, Landolt-Börstein, New Series **III/19d2**, 248 (1990).
- [84] J. H. K. Buschow, *Rep. Prog. Phys.* **42**, 1373 (1979)
- [85] T. Tolinski, W. Schäfer, A. Kowalczyk, B. Andrzejewski, A. Hoser and A. Szlaferek, *J. Alloys Comp.* **385**, 28 (2004)
- [86] M. Coldea, V. Pop, M. Neumann, O. Isnard and L.G. Pășcuț, *J. Alloys Comp.* **390**, 16 (2005)
- [87] Ch. Müller, H. Wonn, W. Blau, P. Ziesche and P. V. Krivitshii, *Phys Stat Sol.* **B 95**, 215 (1979)
- [88] L. Rednic, M.Coldea, V. Rednic, M. Neumann, D. Benea, *Studia Physica 2*, 65-71 (2008)
- [89] H. J. Williams, R. C. Sherwood, F. G. Foster, and E. M. Kelley, *J. Appl. Phys.* **28**, 1181(1957)
- [90] C. Guillard, *J. Phys Radium* **12**, 143 (1951)
- [91] J. B. Yang, K. Kamaraju, W.B. Yelon, W. J. James, *Appl. Phys. Lett.* **79**, 1846 (2001)
- [92] P.M. Oppeneer, V.N. Antonov, T. Kraft, H. Eschrig, A.N. Yaresko, A.Ya. Perlov, *J. Appl. Phys.* **80**, 1099. (1996)
- [93] R. Coehoorn and R. A. De Groot, *J. Phys. F: Met. Phys.* **15**, 2135 (1985)
- [94] H. Yoshida, T. Shima, T. Takahashi, H. Fujimori, *Mater. Trans. JIM* **40**, 455 (1999)
- [95] X. Guo, Z. Altounian, J.O. Stom-Olsen, *J. Appl. Phys.* **69**, 6067 (1991).
- [96] S. Saha, M.Q. Huang, C.J. Thong, B.J. Zande, V.K. Chandhok, S. Simizu, R.T. Obermyer, S.G. Sankar, *J. Appl. Phys.* **87**, 6040 (2000)
- [97] Y. J. Wang, *J. Magn. Magn. Mater.* **84**, 39 (1990)
- [98] P. Bandaru, T. D. Sands, Y. Kubota, and E. E. Marinero, *Appl. Phys. Lett.* **72**, 1 (1998)
- [99] R. F. Sabiryanov and S. S. Jaswal, *J. Appl. Phys.* **85**, 8 (1999)
- [100] R. Coehoorn, C. Haas and R.A. de Groot, *Phys. Rev. B* **31**, 1980 (1990)
- [101] F. Heusler, *Z. Angew Chem.* **17**, 260 (1904)
- [102] K. Thielman, *Ann. Physik* **137**, 41 (1940)
- [103] C. Guillaud, Thesis, University of Strasbourg, France (1943)

- [104] S. Saha, R. T. Obermyer, B. J. Zande, V. K. Chandhok, S. Simizu and S. G. Sankar, *J. Appl. Phys.* **91**(10), 8525 (2002)
- [105] Ruixuan Dai, NuoFu Chen, X. W. Zhang and Changtao Peng, *Journal of Crystal Growth* **299**(1), 142 (2007)
- [106] Ph. Wernet, B. Sonntag, M. Martins, P. Glatzel, B. Obst and P. Zimmermann, *Phys. Rev. A* **63**, 050702(R) (2001)

ACKNOWLEDGEMENTS

First of all I would especially like to thank to my supervisor, **Prof. Dr. Marin Coldea**, for his constant and invaluable support. Each time an interesting scientific question came up, his appeal for insight discussions and interpretation of the experimental data results helped me move on and gave me valuable hints. His encouragement and advices consistently assisted my work during *PhD* period.

My special thanks and gratitude go to **apl. Prof. Prof.h.c. Dr. Dr.h.c. Manfred Neumann**, not only for accepting to be part of my *PhD* commission and to referee my work, but also for his hospitality and financial support during all my stages at Osnabrück University. The long and nice discussions we have had about *X-Ray Photoelectron Spectroscopy* were a real help in order to clarify different aspects with regard to this research field.

I am deeply indebted to **Prof. Dr. Viorel Pop**, for guiding me through the field of magnetism ever since I was a student. The very interesting and fruitful discussions helped me clarify several underlying aspects concerning magnetic behaviour. He is also acknowledged for the magnetic measurements performed at *Laboratoire de Crystallographie CNRS, Grenoble* and *Institute des Matériaux Jean Rouxel, Nantes*.

I would like to give a special thank to **senior research scientist Rodica Paula Turcu**, for refereeing my thesis.

My thanks go also to Prof. Dr. Iosif G. Deac and Dr. Eugen Dorolti for our collaboration in the field of magnetic semiconductors and to Dr. Diana Benea for performing the band structure calculations. Senior research scientist Nicolae Aldea is also acknowledged for performing X-ray diffraction line profile approximations.

Former and actual colleagues are acknowledged for the very pleasant working atmosphere: Roxana, Daniel, Iulian, Calin and Adrian. It has been a pleasure to share the office with Dr. Daniel Andreica and Roxana, thank you both for the many constructive discussions.

At last, but not least, I am grateful to my husband Vasile who was beside me in all, encouraging me, supporting me and having a lot of patience. To my parents I would like to thank them for their trust and for their constant support provided during my studies. They were and continue being always beside me in everything.